Direct Evidence of Mechanical and Radiative AGN Feedback in IRAS 09104+4109

K. W. Cavagnolo[1,2,3]⋆, M. Donahue[2], G. M. Voit[2], B. R. McNamara[1,4,5], and M. Sun[6]

[1]*University of Waterloo, Waterloo, ON, Canada.*
[2]*Michigan State University, East Lansing, MI, USA.*
[3]*Observatoire de la Côte d'Azur, Nice, PACA, France.*
[4]*Perimeter Institute for Theoretical Physics, Waterloo, ON, Canada.*
[5]*Harvard-Smithsonian Center for Astrophysics, Cambridge, MA, USA.*
[6]*University of Virginia, Charlottesville, VA, USA.*

ABSTRACT

Using observations from the *Chandra* X-ray Observatory, we present a detailed study of the ultraluminous infrared brightest cluster galaxy IRAS 09104+4109 and the surrounding intracluster medium (ICM) of the host galaxy cluster RX J0913.7+4056. The X-ray data reveals cavities formed by $\sim 10^{44}$ erg s^{-1} jets from the $> 4 \times 10^{46}$ erg s^{-1} buried quasar in IRAS 09104+4109, and excess X-ray emission near the core which is well-modeled as illumination of the ICM and a galactic nebula by the quasar. Consistent with previous studies, we show that the X-ray properties of the IRAS 09104+4109 nucleus are dominated by reflected emission from a quasar embedded in a moderately Compton-thick medium. Our interpretation of the observations suggest IRAS 09104+4109 may be a local example of how higher-redshift galaxies transition from a radiatively-dominated (*i.e.* quasar-mode) to a mechanically-dominated (*i.e.* radio-mode) form of feedback.

Key words: cooling flows – galaxies: clusters: galaxies: individual (IRAS 09104+4109): clusters: individual (RX J0913.7+4056)

1 INTRODUCTION

The discovery of tight correlations between various properties of a galaxy and the mass of its centrally located supermassive black hole (SMBH) strongly indicate that the two co-evolve (*e.g.* Kormendy & Richstone 1995; Magorrian et al. 1998; Ferrarese & Merritt 2000; Gebhardt et al. 2000; Graham et al. 2001). It has been suggested that galaxy mergers and interactions, along with feedback from an active galactic nucleus (AGN), form the foundation for SMBH-host galaxy co-evolution (*e.g.* Binney & Tabor 1995; Silk & Rees 1998; Kauffmann & Haehnelt 2000; Granato et al. 2001). The most massive galaxies in the universe, *e.g.* brightest cluster galaxies (BCGs), are a unique population in the co-evolution framework as their properties are also correlated with the galaxy cluster, or group, in which they reside (*e.g.* Jones & Forman 1984; Dubinski 1998). Thus, BCGs are especially valuable for investigating galaxy formation and evolution processes in a cosmological context, and in this paper we discuss one rare BCG, IRAS 09104+4109 (hereafter I09), which may be providing vital clues about these processes.

Galaxy formation models typically segregate AGN feedback into a distinct early-time, radiatively-dominated quasar mode (*e.g.* Springel et al. 2005; Hopkins et al. 2006) and a late-time, mechanically-dominated radio mode (*e.g.* Croton et al. 2006; Bower et al. 2006). During the quasar mode of feedback, it is believed that quasar radiation couples to nearby gas and drives strong winds which deprive the SMBH of additional fuel, regulating growth of black hole mass (*e.g.* Hopkins et al. 2005; Di Matteo et al. 2005). This phase is expected to be short-lived, resulting in the expulsion of gas from the host galaxy and temporarily quenching star formation (*e.g.* Narayanan et al. 2006; Menci et al. 2008). Direct evidence of radiative AGN feedback has been elusive (see Veilleux et al. 2005, for a review), with only a handful of systems (*e.g.* Polletta et al. 2008; Feruglio et al. 2010) and low-redshift ellipticals (Schawinski et al. 2009) providing the strongest evidence to date that quasar feedback influences the host galaxy in the ways models predict.

At later times, when quasar activity has faded and radio mode feedback takes over, SMBH launched jets regulate the growth of galaxy mass through prolonged and intermittent mechanical heating of a galaxy's gaseous halo (Kereš et al. 2005; Dekel & Birnboim 2006; McNamara & Nulsen 2007). Direct evidence of mechanical AGN feedback is seen in the form of cavities and shocks found in the X-ray halos of many massive galaxies (*e.g.* Churazov et al. 2001; Forman et al. 2007), particularly in the relatively dense ICM surrounding most BCGs (*e.g.*

⋆ Email: kcavagno@uwaterloo.ca

Fabian et al. 2000b; McNamara et al. 2000). Encouragingly, these cavities and shocks have been shown to contain enough energy to offset much of the halo cooling (Fabian et al. 2003; Bîrzan et al. 2004; Dunn & Fabian 2006; Rafferty et al. 2006). However, how cavity energy is thermalized remains unclear (Mathur et al. 2009; De Young et al. 2008).

Models breakdown AGN feedback into two generic modes for simplicity, but they still form a unified schema (*e.g.* Sijacki et al. 2007) which predicts a continuous distribution of AGN luminosities (*e.g.* Hopkins & Hernquist 2009). However, the association of the two generic AGN modes, and whether they interact, is still poorly understood, partly from a lack of observational constraints. This paper presents evidence that the AGN in I09 is producing both mechanical and radiative feedback, perhaps implying that it is transitioning between the dominant mode of feedback, providing a local example of how massive galaxies at higher redshifts evolve from quasar-mode into radio-mode.

I09 is an uncommon, low-redshift ($z = 0.4418$) ultraluminous infrared galaxy (ULIRG; $L_{IR} \sim 10^{13}\ L_\odot$). Unlike most ULIRGs, I09 is the BCG in a rich galaxy cluster, but unlike most BCGs, the spectral energy distribution (SED) of I09 is dominated by a heavily obscured quasar: it has the optical spectrum of a Seyfert-2 with most of the bolometric luminosity emerging longward of 1 μm (Kleinmann et al. 1988; Hines & Wills 1993; Fabian et al. 1994; Evans et al. 1998; Franceschini et al. 2000; Iwasawa et al. 2001). Another interesting feature of I09 is the nearly orthogonal misalignment between the beaming directions of the radio jets and nuclear radiation (Hines et al. 1999, hereafter H99). Using X-ray data from the *Chandra* X-ray Observatory (*CXO*), we present the discovery of jet induced cavities in the X-ray halo surrounding I09, and an unambiguous detection of quasar radiation interacting with cold gas in the galaxy halo. The analysis and discussion that follows focuses primarily on placing I09 into the quasar-mode/radio-mode AGN feedback paradigm and interpreting the misalignment between the radiative and mechanical outflows in terms of this paradigm.

Data reduction is discussed in Section 2. Properties of the ICM are analyzed in Sections 3 and 4. The complex nuclear source is discussed in Section 5. Analysis of the quasar irradiation of the ICM, ICM cavities, and SMBH fueling are given in Sections 6, 7, and 8, respectively. Interpretation of the results are given in Section 9, with a brief summary in Section 10. A ΛCDM cosmology with $H_0 = 70$ km s^{-1} Mpc^{-1}, $\Omega_M = 0.27$, and $\Omega_\Lambda = 0.73$ is adopted, for which a redshift of $z = 0.4418$ corresponds to ≈ 9.1 Gyr for the age of the Universe, $D_A \approx 5.72$ kpc arcsec^{-1}, and $D_L \approx 2.45$ Gpc.

2   OBSERVATIONS

2.1   X-ray

Unless stated otherwise, all X-ray spectral analysis was performed over the energy range 0.7–7.0 keV with the χ^2 statistic in XSPEC 12.4 (Arnaud 1996) using an absorbed, single-temperature MEKAL model (Mewe et al. 1985) with gas metal abundance as a free parameter (Anders & Grevesse 1989 Solar distribution adopted) and quoted uncertainties of 90% confidence. All spectral models had the Galactic absorbing column density fixed at $N_{H,Gal} = 1.58 \times 10^{20}$ cm^{-2} (Kalberla et al. 2005). The ICM mean molecular weight and adiabatic index are assumed to be $\mu = 0.597$ and $\gamma = 5/3$, respectively. The I09 nucleus emits strong Fe Kα emission which affects spectral fitting, and for analysis of the ICM, the nucleus was excluded using a region twice the size of the *CXO*

PSF 90% EEF (see Section 5). The X-ray analysis in this paper relates to *CXO* data only.

2.1.1   CXO

A 77.2 ks *CXO* observation of I09 was taken in January 2009 with the ACIS-I instrument (ObsID 10445), and a 9 ks ACIS-S observation was taken in November 1999 (ObsID 509; PI Fabian). Both datasets were reprocessed and reduced using CIAO and CALDB versions 4.2. X-ray events were selected using *ASCA* grades, and corrections for the ACIS gain change, charge transfer inefficiency, and degraded quantum efficiency were applied. Point sources were located and excluded using WAVDETECT and verified by visual inspection. Light curves were extracted from a source-free region of each observation to look for flares, and time intervals with $> 20\%$ of the mean background count rate were excluded. After flare exclusion, the final combined exposure time is 83 ks.

For imaging analysis, the flare-free events files were reprojected to a common tangent point and summed. The astrometry of the ObsID 509 dataset was improved using a new aspect solution created with the CIAO tool REPROJECT_ASPECT and the positions of several field sources. After astrometry correction, the positional accuracy between both observations improved by $\approx 0.4''$ and was comparable to the resolution limit of the ACIS detectors ($\approx 0.492''$ pix^{-1}). We refer to the final point source free, flare-free, exposure-corrected images as the "clean" images. In Figure 1 are the 0.5–10.0 keV mosaiced clean image of RX J0913.7+4056, a zoom-in of the core region harboring I09, and photons in the energy range 4.35–4.50 keV associated with the Fe Kα fluorescence line from the nucleus (discussed in Section 5).

2.1.2   BeppoSAX

Conclusions reached in previous studies regarding the nature of the obscuring material in the nucleus of I09 have relied on the *BeppoSAX* hard X-ray detection discussed by Franceschini et al. (2000). Here, we repeat and confirm that analysis in order to compare our results in Section 5 against Franceschini et al. (2000). We retrieved and re-analyzed the *BeppoSAX* data taken April 1998 (ObsCode 50273002; PI Franceschini). After reprocessing, we measure a PDS 15–80 keV count rate of 0.106 ± 0.055 ct s^{-1}. Fitting the PDS spectrum over the energy range 20–200 keV with an absorbed power-law having fixed spectral index of $\Gamma = 1.7$ yielded fluxes of $f_{10-200} = 2.09^{+1.95}_{-1.95} \times 10^{-11}$ erg s^{-1} cm^{-2} and $f_{20-100} = 1.10^{+1.57}_{-1.63} \times 10^{-11}$ erg s^{-1} cm^{-2}, in agreement with Franceschini et al. (2000).

2.1.3   INTEGRAL and Swift

I09 was not detected in the *INTEGRAL* IBIS Extragalactic AGN Survey (Bassani et al. 2006, $E_{sens} = 20$–100 keV). Our re-analysis of archival *INTEGRAL* ISGRI and JEM-X data resulted in 3σ upper limits between 10–35 keV and 20–100 keV of $f_{10-35} = 1.28 \times 10^{-12}$ erg s^{-1} cm^{-2} and $f_{20-100} = 5.70 \times 10^{-11}$ erg s^{-1} cm^{-2}, higher than the *BeppoSAX* 20–100 keV PDS measured flux, and consistent with the IBIS Survey non-detection for a $z = 0.44$ source. I09 was also not detected in the 22 month *Swift*-BAT Survey (Tueller et al. 2010, $E_{sens} = 15$–150 keV). The *Swift*-BAT Survey has a 14–195 keV 4.8σ detection limit of 2.2×10^{-11} erg s^{-1} cm^{-2}, higher than the 14–195 keV I09 flux expected based on the *BeppoSAX* detection. Assuming the upper limits are

representative of an $\approx 1°$ region around I09 (*i.e.* the full-width half maximum PDS field of view), the lack of detected hard X-ray sources near I09 suggests that the PDS detection did not originate from a brighter off-axis source, assuming the source is not transient or was a one-time event.

2.2 Radio

2.2.1 Data Reduction

Between 1986 and 2000, I09 was observed with the Very Large Array (*VLA*) at multiple radio frequencies and resolutions (see also Hines & Wills 1993, for 1.4 and 5 GHz analysis; hereafter H93). Continuum mode observations were taken from the *VLA* archive and reduced using version 3.0 of the Common Astronomy Software Applications (CASA). Flagging of bad data was performed using a combination of CASA's FLAGDATA tool in RFI mode and manual inspection. Radio images were generated by Fourier transforming, cleaning, self-calibrating, and restoring individual radio observations. The additional steps of phase and amplitude self-calibration were included to increase the dynamic range and sensitivity of the radio maps. All sources within the primary beam and first side-lobe detected with fluxes $\geqslant 5\sigma_{rms}$ were imaged to further maximize the sensitivity of the radio maps.

Resolved radio emission associated with I09 is detected at 1.4 GHz, 5.0 GHz, and 8.4 GHz, while a 3σ upper limit of 0.84 mJy is established at 14.9 GHz. Fluxes for unresolved emission at 74 MHz, 151 MHz, and 325 MHz were retrieved from VLSS (Cohen et al. 2007), 7C Survey (Riley et al. 1999), and WENSS (Rengelink et al. 1997), respectively. No formal detection is found in VLSS, however, an overdensity of emission at the location of I09 is evident. For completeness, we measured a flux for the potential source, but excluded the value during fitting of the radio spectrum.

The combined 1.4 GHz image is the deepest and reveals the most extended structure, thus our discussion regarding radio morphology is guided using this frequency. The deconvolved, integrated 1.4 GHz flux of the continuous extended structure coincident with I09, and having $S_\nu \gtrsim 3\sigma_{rms}$, is 14.0 ± 0.51 mJy. A significant spur of radio emission extending northeast from the nucleus is detected with flux 0.21 ± 0.07 mJy. Radio contours were generated beginning at 3 times the rms noise and moving up in 6 log-space steps to the peak intensity of 4.7 mJy beam^{-1}. These are the contours referenced in all following discussion of the radio source morphology and its interaction with the X-ray gas.

2.2.2 Source Analysis

Below we discuss properties of the radio source for the later purpose of better understanding the AGN outflow which created cavities in the X-ray halo around I09 (see Section 7). The radio spectrum was fitted between 151 MHz and 8.4 GHz for the full radio source (lobes, jets, and core) with the well-known KP (Kardashev 1962; Pacholczyk 1970), JP (Jaffe & Perola 1973), and CI (Heavens & Meisenheimer 1987) synchrotron models. The models primarily vary in their assumptions regarding the electron pitch-angle distribution and number of particle injections. The models were fitted to the radio spectrum using the code of Waters & Zepf (2005), which is based on the method of Carilli et al. (1991). The JP model (single electron injection, randomized but isotropic pitch-angle distribution) yields the best fit with χ^2(DOF)= 4.91(3), a break frequency of $\nu_B = 12.9 \pm 1.0$ GHz, and a low-frequency ($\nu < 2$ GHz) spectral index of $\alpha =$

-1.10 ± 0.09. The bolometric radio luminosity was approximated by integrating under the JP curve between $\nu_1 = 10$ MHz and $\nu_2 = 10,000$ MHz, giving $L_{radio} = 1.09 \times 10^{42}$ erg s^{-1}. The radio spectrum and best-fit models are shown in Figure 2.

Assuming inverse-Compton (IC) scattering and synchrotron emission are the dominant radiative mechanisms of the radio source, the time since acceleration for an isotropic particle population is given by Slee et al. (2001) as

$$t_{sync} = 1590 \left(\frac{B^{1/2}}{B^2 + B_{CMB}^2} \right) [\nu_B(1+z)]^{-1/2} \text{ Myr} \qquad (1)$$

where B [μG] is magnetic field strength, $B_{CMB} = 3.25(1+z)^2$ [μG] is a correction for IC losses to the cosmic microwave background, ν_B [GHz] is the radio spectrum break frequency, and z is the dimensionless source redshift. Note that this form for t_{sync} neglects energy lost to adiabatic expansion of the radio plasma (Scheuer & Williams 1968). We assume that B is not significantly different from the equipartition magnetic field strength, B_{eq} (see Bîrzan et al. 2008, for thorough discussion of the validity and shortcomings of this assumption), which is derived from the minimum energy density condition as (Miley 1980)

$$B_{eq} = \left[\frac{6\pi c_{12}(\alpha, \nu_1, \nu_2) L_{radio} (1+k)}{V\Phi} \right]^{2/7} \mu\text{G} \qquad (2)$$

where $c_{12}(\alpha, \nu_1, \nu_2)$ is a dimensionless constant (Pacholczyk 1970), L_{radio} [erg s^{-1}] is the integrated radio luminosity from ν_1 to ν_2, k is the dimensionless ratio of lobe energy in non-radiating particles to that in relativistic electrons, V [cm^3] is the radio source volume, and Φ is a dimensionless radiating population volume filling factor. Synchrotron age as a function of k and Φ for the full radio source is shown in Figure 2. For various combinations of k and Φ, $B_{eq} \approx 4$–57 μG, with associated synchrotron ages in the range ≈ 1–12 Myr, typical of other BCG radio sources (*e.g.* Bîrzan et al. 2008). Repeating the above analysis using only radio lobe emission at 1.4 GHz, 5.0 GHz, and an 8.4 GHz upper limit reveals $t_{sync} \sim 30$ Myr resulting from a significantly steeper spectral index and lower break frequency.

3 GLOBAL ICM PROPERTIES

Our analysis begins at the cluster scale with the integrated properties of the RX J0913.7+4056 ICM hosting I09. We define the mean cluster temperature, T_{cl}, as the ICM temperature within a core-excised aperture extending to R_{Δ_c}, the radius at which the average cluster density is Δ_c times the critical density for a spatially flat Universe. We chose $\Delta_c = 500$ and used the relations from Arnaud et al. (2002) to calculate R_{Δ_c}. RX J0913.7+4056 has a luminous, cool core and complex nucleus (see Section 5) which are not representative of T_{cl}, thus, the convention of Maughan (2007) was followed and emission inside $0.15 R_{500}$ was excised. Source spectra were extracted from the region 0.15–$1.0 R_{500}$ and background spectra were extracted from reprocessed CALDB blank-sky backgrounds (see Section 4). Because T_{cl} and R_{Δ_c} are correlated in the adopted definitions, they were recursively determined until three consecutive iterations produced T_{cl} values which agreed within the 68% confidence intervals. We measure $T_{cl} = 7.54^{+1.76}_{-1.15}$ keV corresponding to $R_{500} = 1.16^{+0.27}_{-0.19}$ Mpc. Measurements for other R_{Δ_c} apertures are given in Table 1.

The cluster gas and gravitational masses were derived using the deprojected radial electron density and temperature profiles presented in Section 4. Because the radial temperature and density

profiles extend to $\approx 0.2R_{200}$, the gravitating and gas mass calculations below include significant extrapolation, and thus may be lower limits, though their ratio should not be significantly different. Electron gas density, n_e, was converted to total gas density as $n_g = 1.92n_e\mu m_H$ where m_H [g] is the mass of hydrogen. The gas density profile was fitted with a β-model (Cavaliere & Fusco-Femiano 1978), and the temperature profile was fitted with the 3D-$T(r)$ model of Vikhlinin et al. (2006) to ensure continuity and smoothness of the radial log-space derivatives when solving the hydrostatic equilibrium equation. Total gas mass was calculated by assuming spherical symmetry and integrating the best-fit β-model out to R_{200}, giving $M_{gas}(r < R_{200}) = 7.99\ (\pm0.65) \times 10^{13}$ M$_\odot$. The gravitating mass was derived by solving the hydrostatic equilibrium equation using the analytic density and temperature profiles. We calculate $M_{grav}(r < R_{200}) = 7.22\ (\pm1.44) \times 10^{14}$ M$_\odot$, giving a ratio of gas mass to gravitating mass of 0.11 ± 0.02. The gas and gravitating mass errors were estimated from 10,000 Monte Carlo realizations of the measured density and temperature profiles and their associated uncertainties.

With the exception of the strange BCG at its heart, RX J0913.7+4056 appears to be a typical massive, relaxed galaxy cluster. The integrated X-ray cluster properties give no indication to suspect the system has experienced a major event which may have dramatically disrupted the ICM. RX J0913.7+4056 has a temperature, luminosity, and gas fraction consistent with flux-limited and representative cluster samples (Reiprich & Böhringer 2002; Pratt et al. 2009), implying that the peculiar nature of I09 does not arise from the galaxy residing in a special or atypical cluster. Adjusted for differences in assumed cosmology, our global measurements agree with prior studies of I09 (*e.g.* Allen 2000).

4   RADIAL ICM PROPERTIES

Now we discuss the finer global structure of RX J0913.7+4056 via radial ICM profiles. Temperature (kT_X) and abundance (Z) profiles were created using circular annuli centered on the cluster X-ray peak and containing 2500 and 5000 source counts per annulus, respectively. Spectra were grouped to 25 source counts per energy channel. CALDB blank-sky backgrounds were reprocessed and reprojected to match each observation, and then normalized for variations of the hard-particle background using the ratio of blank-sky and observation 9.5–12 keV count rates. Following the method outlined in Vikhlinin et al. (2005), a fixed background component was included during spectral analysis to account for the spatially-varying Galactic foreground (see Cavagnolo et al. 2008b, for more detail). A deprojected temperature profile was generated using the DEPROJ model in XSPEC, but it does not significantly differ from the projected profile. Thus, the projected profile is used in all analysis. The temperature and abundance profiles are shown in the top row of Figure 3.

After masking out all X-ray substructure (see Section 6) and the central 2″, a grouped spectrum for the central 20 kpc was fitted with a thermal model plus a cooling flow component. The best-fit model has a mass deposition rate of $\dot{M} = 206^{+87}_{-65}$ M$_\odot$ for upper and lower temperatures of 5.43 keV and 0.65 keV, respectively, with abundance 0.5 $Z_\odot$. The factor of 3 temperature difference implies there may be interesting soft X-ray ionization lines, but currently there is no grating X-ray spectroscopy of I09.

A surface brightness (SB) profile was extracted using concentric 1″ wide circular annuli centered on the cluster X-ray peak. From the SB and temperature profiles, a deprojected electron den-

sity (n_e) profile was derived using the Kriss et al. (1983) technique (see Cavagnolo et al. 2009, for more detail). Errors for the density profile were estimated from 10,000 Monte Carlo bootstrap resamplings of the SB profile. The SB and n_e profiles are shown in the second row of Figure 3.

Total gas pressure ($P = nkT_X$), entropy ($K = kT_X n_e^{-2/3}$), cooling time ($t_{cool} = 3nkT_X\ [2n_e n_H \Lambda(T,Z)]^{-1}$), and enclosed X-ray luminosity (L_X) profiles were also created, where $n = 2.3n_H$, $n_H = n_e/1.2$, and $\Lambda(T,Z)$ is a cooling function. These profiles are presented in the bottom two rows of Figure 3. Uncertainties for each profile were calculated by propagating the individual parameter errors and then summing in quadrature. The cooling functions were derived from the best-fit spectral model for each annulus of the temperature profile and linearly interpolated onto the grid of the higher resolution density profile. The function $K(r) = K_0 + K_{100}(r/100\ \text{kpc})^\alpha$ was fitted to the entropy profile, giving best-fit values of $K_0 = 12.6\pm2.9$ keV cm^2, $K_{100} = 139\pm8$ keV cm^2, and $\alpha = 1.71\pm0.10$.

There are no resolved discontinuities in the kT_X, n_e, or P profiles to suggest the presence of a shock or cold front. Additional 2D analysis using the weighted Voronoi tessellation and contour binning methods of Diehl & Statler (2006) and Sanders (2006), respectively, also did not reveal any significant temperature or abundance substructure. The ICM structure is typical of the cool core class of galaxy clusters (*e.g.* Cavagnolo et al. 2009; Sanderson et al. 2009) and the population of $K_0 < 30$ keV cm^2 clusters that have radio-loud AGN and star formation in the BCG (Cavagnolo et al. 2008a; Rafferty et al. 2008). Again, RX J0913.7+4056 appears to be a perfectly ordinary cluster, sans the presence of I09.

We point out that the $K_0 \lesssim 30$ keV cm^2 scale defines an interesting entropy regime in which thermal electron conduction in cluster cores is suspected of being too inefficient to suppress widespread environmental cooling (Voit et al. 2008). Therefore, cooling subsystems, like gas ram pressure stripped from cluster members or ICM thermal instabilities, should be long-lived. Consistent with this picture, there is an abundance of cool, gaseous substructure surrounding I09, and in Section 8 we discuss the possible relation of this structure to the AGN activity.

5   I09 NUCLEUS PROPERTIES

5.1   Spectral Analysis

The central I09 X-ray source excluded from the global and radial analyses is analyzed in detail in this section. The centroid and extent of the source were determined using the CIAO tool `wavdetect` and the *CXO* PSF. Each was confirmed with a hardness ratio map, shown in Figure 4, calculated as $HR = f(2.0–9.0\ \text{keV})/f(0.5–2.0\ \text{keV})$, where f is the flux in the denoted energy band. The source is point-like, so a source extraction region was defined using the 90% enclosed energy fraction (EEF) of the normalized *CXO* PSF specific to the nuclear source median photon energy and off-axis position. The elliptical source region had an effective radius of $1.16''$. A segmented elliptical annulus with the same central coordinates, ellipticity, and position angle as the source region, but having 5 times the area, was used for the background region. The background annulus was broken into segments to avoid the regions of excess X-ray emission discussed in Section 6. The HR map and extraction regions are shown in Figure 4. Source and background spectra were created using the CIAO

tool `psextract` for each *CXO* observation and grouped to have 20 counts per energy channel. Approximately 72% of the 2009 spectrum (hereafter SP09) is from the source, with a count rate of $1.63 (\pm 0.06) \times 10^{-2}$ ct s^{-1} in the 0.5–9.0 keV band. For the 1999 spectrum (hereafter SP99), 67% is source flux, with a 0.5–9.0 keV count rate of $2.71 (\pm 0.26) \times 10^{-2}$ ct s^{-1}.

Previous studies have shown the nuclear spectrum is best modeled as Compton reflection from cold matter with a strong Fe Kα fluorescence line at $E_{\rm rest} = 6.4$ keV (*e.g.* Iwasawa et al. 2001). SP99 and SP09 were fitted separately in XSPEC over the energy range 0.5–7.0 keV with an absorbed PEXRAV model (Magdziarz & Zdziarski 1995) plus three Gaussians to account for the Fe Kα line and two additional line-like features around 0.8 keV and 1.3 keV (see also Iwasawa et al. 2001). The disk-reflection geometry employed in the PEXRAV model is not ideal for fitting reflection from a Compton-thick torus (Murphy & Yaqoob 2009), but no other suitable XSPEC model is currently available. Hence, only the reflection component of the PEXRAV model was used and the power law had no high energy cut-off. Fitting separate SP99 and SP09 models also allowed for source variation in the decade between observations, however Γ was poorly constrained for SP99 and thus fixed at the SP09 value. Using constraints from Taniguchi et al. (1997) and Tran et al. (2000), the model parameters for reflector abundance and source inclination were fixed at 1.0 Z$_\odot$ and $i = 50°$, respectively. The best-fit model parameters are given in Table 2, and the background-subtracted spectra overplotted with the best-fit models are presented in Figure 4.

5.2 Emission Lines

Strong Mg, Ne, S, and Si Kα fluorescence lines at $E < 3.0$ keV can be present in reflection spectra (George & Fabian 1991), as can Fe L-shell lines from photoionized gas (Band et al. 1990). Given that the QSO is extremely luminous and that the spectrum is reflection-dominated, we find it likely that the soft X-ray emission fitted by the two separate Gaussians represents some combination of these emission lines. Using a solar abundance thermal component in place of the two low-energy Gaussians yielded a statistically worse fit. The model systematically underestimated the 1–1.5 keV flux and overestimated the 2–4 keV flux. Leaving the thermal component abundance as a free parameter resulted in 0.1 Z$_\odot$, *i.e.* the thermal component tended toward a featureless, skewed-Gaussian.

The equivalent width of the Fe Kα line (EW$_{\rm K\alpha}$) is a valuable diagnostic for probing the environment of an AGN (see Fabian et al. 2000a, for a review). Our measurement of EW$_{\rm K\alpha}$ agrees with previous studies which found EW$_{\rm K\alpha} \lesssim 1$ keV (Franceschini et al. 2000; Iwasawa et al. 2001; Piconcelli et al. 2007), but the large uncertainties prevent us from determining if EW$_{\rm K\alpha}$ has varied since 1998. Our results are also consistent with models and observations which show that EW$_{\rm K\alpha} \gtrsim 0.5$ keV is correlated with $\Gamma \gtrsim 1.7$ and reflecting column densities $N_{\rm H,ref} \sim 10^{24}$ cm^{-2} (Matt et al. 1996; Nandra et al. 1997; Zdziarski et al. 1999; Guainazzi et al. 2005).

5.3 Obscuring Screen

Previous studies of I09 suggested the *BeppoSAX* PDS detection resulted primarily from transmission of hard X-rays through an obscuring screen with a column density $N_{\rm H,obs} > 10^{24}$ cm^{-2}. Extrapolating our best-fit model out to 10–80 keV reveals statistically acceptable agreement with the PDS data (see Figure 5), indicating no transmitted component is necessary. The 10–200 keV

flux of our best-fit reflection-only model is $f_{10-200} = 8.15^{+0.21}_{-0.19} \times 10^{-12}$ erg s^{-1} cm^{-2}, which is not significantly different from the 10–200 keV flux measured with *BeppoSAX*.

If transmitted hard X-ray emission is present in the 0.5–7.0 keV range selected for spectral analysis, the best-fit power-law component will be artifically shallower than its intrinsic value, and the reflected hard X-ray flux will thus be overestimated. However, we tested this possibility using simulated spectra and found that for $\Gamma \geqslant 1.7$, column densities $> 3 \times 10^{24}$ cm^{-2} are sufficient to suppress significant transmitted emission below our 7 keV spectral analysis cut-off, indicating the best-fit model should not have an artificially low Γ. Consistent with this result, addition of an absorbed, power-law component to the modeling lowered χ^2 (best-fit $N_{\rm H,obs} = 3 \times 10^{24}$ cm^{-2} and $\Gamma = 1.7$), but with no improvement to the goodness of fit derived from 10,000 Monte Carlo simulations.

That we find no need for an additional hard X-ray component does not contradict the well-founded conclusion that I09 harbors a Compton-thick quasar. On the contrary, the measured EW$_{\rm K\alpha}$ suggests reflecting column densities of $N_{\rm H,ref} \sim 1–5 \times 10^{24}$ cm^{-2} (Leahy & Creighton 1993; Guainazzi et al. 2005; Comastri et al. 2010). Assuming the density of material surrounding the quasar is mostly homogeneous, *i.e.* $N_{\rm H,ref} \approx N_{\rm H,obs}$, our results are consistent with the presence of a moderately Compton-thick obscuring screen.

5.4 Intrinsic Quasar Luminosity

The 2–10 keV *reflected* flux of our best-fit model without Galactic absorption is $4.24^{+0.57}_{-0.55} \times 10^{-13}$ erg s^{-1} cm^{-2}, corresponding to a rest-frame luminosity $L^{\rm refl}_{2-10} = 1.57^{+0.19}_{-0.19} \times 10^{44}$ erg s^{-1} and bolometric (0.01–100.0 keV) luminosity $L^{\rm refl}_{\rm bol} = 4.20^{+0.49}_{-0.47} \times 10^{45}$ erg s^{-1}. Since the reflection component is the only directly measured quantity, the intrinsic quasar luminosity, $L^{\rm QSO}_{\rm bol}$, can only be infered. If the reflector scattering albedo is $\eta \lesssim 0.1$, a reasonable assumption for systems with properties like I09 (Murphy & Yaqoob 2009), then $L^{\rm QSO}_{\rm bol} \gtrsim 4 \times 10^{46}$ erg s^{-1}. Since the reflector solid angle exposed to our line of sight is highly uncertain, the true luminosity may be more than twice this value, possibly $\sim 10^{47}$ erg s^{-1}. These values are consistent with I09's 0.3–70μm luminosity of $\approx 5 \times 10^{46}$ erg s^{-1} (Kleinmann et al. 1988, H99) which is attributed to dust reprocessing of quasar radiation. Hereafter, we assume that $L^{\rm QSO}_{\rm bol} \approx 8 \times 10^{46}$ erg s^{-1}.

6 QUASAR RADIATIVE FEEDBACK

6.1 ICM X-ray Excesses

Shown in Figure 5 is a residual X-ray image of the ICM which reveals three regions with X-ray emission in excess of the best-fit ICM SB model (residual imaging discussed in Section 7). Each region is named according to its location relative to the nucleus: northern excess (NEx), eastern excess (EEx), and western excess (WEx). Below, we discuss the relation of each excess with energy released by the AGN.

A source spectrum was created for each region, and a background spectrum was extracted from regions neighboring each excess which did not show enhanced emission in the residual image. For each region, the ungrouped source and background spectra were differenced within XSPEC and fit with XSPEC's modified Cash statistic (Cash 1979), appropriate for low-count, background-subtracted spectra (see XSPEC Manual Appendix B

and Nousek & Shue 1989; Valtchanov et al. 2004; Balestra et al. 2007; Baldi et al. 2007; Ehlert & Ulmer 2009). During spectral analysis, metal abundance was fixed at 0.5 $Z_\odot$ because the low signal-to-noise (SN) of each residual spectrum prohibited setting it as a free parameter. The best-fit spectral models are given in Table 3.

Analysis of the NEx spectrum was inconclusive due to extremely low SN, and the WEx has a residual spectrum consistent with thermal emission. The northern radio jet terminates in the NEx region, and the hardness ratio map (see Figure 5) shows a possible hot spot in this same area. The NEx may result from the presence of a very hot thermal phase in the hot spot, or be simply non-thermal emission. Alternatively, the NEx and WEx may be a tenuous, arc-like filament of cool gas displaced by the NW radio jet. Unfortunately the data limits our ability to test these hypotheses spectroscopically.

The EEx spectrum was poorly fit by any combination of thermal models because of prominent emission features at $E < 2$ keV. The EEx thermal Fe Kα complex was also poorly fit because of an obvious asymmetry toward lower energies. To reconcile the poor fit, three Gaussians were added to the EEx model. Comparison of goodness of fits determined from 10,000 Monte Carlo simulations of the best-fit spectra suggest the model with the Gaussians is preferred. Below, we further discuss the EEx exclusively.

6.2 Quasar Irradiation of the ICM and a Nebula

H93 and H99 suggest the AGN which produced the large-scale jets has been reoriented within the last few Myrs, resulting in a new beaming direction close to the line of sight and at roughly a right angle to the previous beaming axis. Interestingly, the new AGN axis suggested by H99 is coincident with the EEx, the radio spur northeast of the radio core, a cone of UV ionization, an ionized optical nebula, and highly polarized diffuse optical emission. These respective features are outlined in Figure 5. Russell et al. (2010) demonstrate that the quasar in H1821+643 is capable of photoionizing gas up to 30 kpc from the nucleus, and we suspect a similar process may be occurring in I09.

To test this hypothesis, reflection and diffuse spectra were simulated for the nebula and ICM coincident with the EEx using CLOUDY (Ferland et al. 1998). The nebular gas density and ionization state were taken from Tran et al. (2000), while the initial ICM temperature, density, and abundance were set at 3 keV, 0.04 cm^{-3}, and 0.5 $Z_\odot$, respectively. No Ca or Fe lines are detected from the nebula coincident with the EEx, possibly as a result of metal depletion onto dust grains (*e.g.* Donahue & Voit 1993), while strong Mg, Ne, and O lines are (Tran et al. 2000). Thus, a metal depleted, grain-rich, 12 kpc thick nebular slab was placed 15 kpc from an attenuated $\Gamma = 1.7$ power law source with power 8×10^{46} erg s^{-1}. Likewise, a 17 kpc × 16 kpc ICM slab was placed 19 kpc from the same source. The quasar radiation was attenuated using a 15 kpc column of density 0.06 cm^{-3}, abundance 0.5 $Z_\odot$, and temperature 3 keV. The output models were summed, folded through the *CXO* responses using XSPEC, and normalized to the observed EEx spectrum (shown in Figure 6).

In the energy range 0.1–10.0 keV, the nebula emission lines which exceed thermal line emission originate from Si, Cl, O, F, K, Ne, Co, Na, and Fe and occur as blends around redshifted 0.4, 0.6, 0.9, and 1.6 keV. The energies and strengths of these blends are in good agreement with the EEx spectrum. Further, the Fe Kα emission from the nebula is 100 times fainter than that from the ICM, and the observed asymmetry of the EEx Fe Kα emission results

from the 6.4 keV Fe Kα photoionized line of the ICM. The consistency of the irradiation model with the observed EEx spectrum, and the coincidence with other emission features like the radio spur, strongly suggests that beamed quasar radiation is responsible for the nature of the EEx. However, whether the irradiation equates to heating of the gas is unclear.

7   AGN MECHANICAL FEEDBACK

7.1   Discovery of ICM Cavities

The I09 X-ray and radio emission morphologies are suggestive of interaction between the halo and jets. To aid investigation of any relationship, a residual X-ray image was created by subtracting a SB model for the ICM from the *CXO* clean image. The *CXO* clean image was binned by a factor of 2 and the SB isophotes were fitted using the IRAF tool ELLIPSE. The geometric parameters ellipticity (ε), position angle (ϕ), and centroid (C) were initially free to vary, but the best-fit values for each isophote converged to mean values of $\varepsilon = 0.14$, $\phi = -76°$, and C [J2000] = (09:13:45.5; +40:56:28.4). These values were fixed in the fitting routine to eliminate the isophotal twisting resulting from statistical variation of the best-fit values for each radial step. The SB model was subtracted from the clean image, resulting in the residual image shown in Figure 5.

The faint SB decrements NW and SE of the nucleus in the clean image are resolved into cylindrical voids in the residual image. The void and radio jet morphologies closely trace each other, confirming they share a common origin in the AGN outburst. Cavities are a well-known phenomenon, but currently, I09 is the highest redshift object where cavities have been directly imaged. In addition, I09 is thus far the only example of a quasar-dominated system with an unambiguous cavity detection. Using a 1994 *ROSAT* HRI observation, Fabian & Crawford (1995) found a "hole" in the core of RX J0913.7+4056 which they attributed to absorption by a > 1000 M$_\odot$ yr^{-1} cooling flow. Neither the cavities nor the hole are seen in a longer 1995 *ROSAT* HRI observation, and when juxtaposed with the *CXO* residual image, the hole in the 1994 *ROSAT* observation is not associated with the cavities.

7.2   Outburst Energetics

The AGN outburst energetics were investigated using properties of the cavities (see McNamara & Nulsen 2007, for a review). Cavity volumes, V, were calculated by approximating each void in the X-ray image with a right circular cylinder projected onto the plane of the sky along the cylinder radial axis. The lengthwise axis of the cylinders were assumed to lie in a plane perpendicular to the line of sight that passes through the central AGN. The energy in each cavity, $E_{cav} = \gamma PV/(\gamma - 1)$, was estimated by assuming the contents are a relativistic plasma ($\gamma = 4/3$), and then integrating the total gas pressure, P, over the surface of each cylinder. The radio source morphology, spectrum, and age suggest the jets were recently being fed by the central AGN. Thus, we assumed the cavities were created on a timescale dictated by the ambient gas sound speed, t_{sonic} (see Bîrzan et al. 2004). The distance the AGN outflow has traveled to create each cavity was set to the cylinder length, not the midpoints, as is common. The power of each cavity is thus $P_{cav} = E_{cav}/t_{sonic}$. Cavity power is often assumed to be a good estimate of the physical quantity jet power, P_{jet}, but note that neither accounts for energy

which may be imparted to shocks (discussed below). Properties of the individual cavities are listed in Table 4.

The total cavity energy and power are estimated at $E_{cav} = 5.11\,(\pm1.33)\times10^{59}$ erg and $P_{cav} = 3.05\,(\pm1.03)\times10^{44}$ erg s^{-1}, respectively. Compared with other systems hosting cavities (*e.g.* Bîrzan et al. 2004; Dunn & Fabian 2008), I09 resides between the middle and upper-end of the cavity power distribution. Radio power, P_{radio}, has been shown to be a reasonable surrogate for estimating mean jet power (Bîrzan et al. 2008), though with considerable scatter. Thus, we checked the P_{cav} calculation using the Cavagnolo et al. (2010) P_{jet}-P_{radio} scaling relations. The relations give $P_{jet} \approx 2–6\times10^{44}$ erg s^{-1}, in agreement with the X-ray measurements, suggesting there is nothing unusual about the ratio of radio to jet power, *i.e.* the implied jet radiative efficiency. The AGN outburst appears to be quite ordinary.

Of interest is how the energy deposited in the cavities compares to the cooling rate of the host X-ray halo. The cooling radius was set at the radius where the ICM cooling time is equal to H_0^{-1} at the redshift of I09. We calculate $R_{cool} = 128$ kpc, and measure an unabsorbed bolometric luminosity within this radius of $L_{cool} = 1.61^{+0.25}_{-0.20}\times10^{45}$ erg s^{-1}. If all of the cavity energy is thermalized over 4π sr, then $\approx 20\%$ of the energy radiated away by gas within R_{cool} is replaced by energy in the observed mechanical outflow. Assuming the mean ICM cooling rate does not vary significantly on a timescale of ~ 1 Gyr, this idealized scenario implies that 5 similar power AGN outbursts will balance the cooling losses of the cluster halo. These are not atypical results for an AGN outburst (*e.g.* Rafferty et al. 2006).

7.3 Constraints on Shock Energy

The P_{cav} estimates neglect the influence of shocks, but the synchrotron age and cavity age are useful in addressing this issue. If t_{sync} is an accurate measure of the radio source age, then the age discrepancy $t_{sonic} \gtrsim 42$ Myr versus $t_{sync} \lesssim 30$ Myr implies the AGN outflow is supersonic. Were it not, the radio-loud plasma will radiate away much of its energy and be mostly radio-quiet prior to reaching the end of the observed jet (neglecting re-acceleration). The implication being that during the cavity creation, some amount of jet kinetic energy may have been imparted to shocks.

Recall that no shocks are detected in the X-ray analysis, and note that the properties of I09 optical emission-line nebulae are inconsistent with excitation due to shocks (Crawford & Vanderriest 1996; Tran et al. 2000). But, the nebular regions studied are $\gtrsim 20$ kpc from the jet axis, and may not be indicative of gas dynamics close to the outflow. Regardless, the energy in possible shocks was crudely estimated by setting $t_{sonic} = 30$ Myr and adjusting P_{cav} by the Mach number: $\Delta P_{cav} = \Delta P / \Delta t$ and $\Delta P \propto M^3$. Relative to the ICM sound speed, the velocity needed to reach the end of the radio jet in 30 Myrs requires a Mach number of ≈ 1.7, which brings the outburst power up to $\approx 3\times10^{45}$ erg s^{-1} ($E_{cav} \approx 2\times10^{60}$ erg for a 30 Myr duration). Within the formal uncertainties, the AGN outburst power is on the order of a few times 10^{44} erg s^{-1}, with the possibility of being as large as 10^{45} erg s^{-1}.

8 FUELING THE FEEDBACK

8.1 Powering the QSO and Jets

An estimate of black hole mass, M_{BH}, is relevant to investigating AGN activity. However, measuring M_{BH} for a BCG is non-

trivial (*e.g.* Dalla Bontà et al. 2009), and M_{BH}-host galaxy relations calibrated using lower mass galaxies may not be relevant above 10^9 M$_\odot$ (Lauer et al. 2007). Acknowledging these difficulties which may yield underestimated M_{BH}, we used the relations in Tremaine et al. (2002) and Graham (2007) which relate M_{BH} with a host galaxy's stellar velocity dispersion and absolute $[B, R, K]$-band magnitudes, respectively. The I09 velocity dispersion, $\sigma_s = 293\pm6$ km s^{-1}, was determined from the Faber & Jackson (1976) relation, and magnitudes were taken from HyperLeda[1], SDSS[2], and 2MASS[3] and corrected using the relations of Cardelli et al. (1989) and Poggianti (1997). The Graham (2007) relations give $M_{BH} \approx 0.6–4.0\times10^9$ M$_\odot$ and the Tremaine et al. (2002) relation gives $M_{BH} \approx 0.6\times10^9$ M$_\odot$. We adopt the weighted mean value of $1.05\,(\pm0.17)\times10^9$ M$_\odot$ where the uncertainty is the error of the mean. The Eddington accretion rate, which is the maximal inflow rate of gas not expelled by radiation pressure, for a black hole of this mass is

$$\dot{M}_{Edd} = \frac{2.2}{\varepsilon}\left(\frac{M_{BH}}{10^9\ M_\odot}\right) \approx 23\ M_\odot\ yr^{-1} \tag{3}$$

where $\varepsilon = 0.1$ is the accretion disk radiative efficiency.

If mass accretion is the dominant power source for the jets (Begelman et al. 1984), and not, for example, SMBH spin (Meier 2002), then jet energy represents some fraction of the gravitational binding energy of material accreting onto the SMBH. Assuming the mass-energy conversion has some efficiency ε, the cumulative cavity energy implies a total accreted mass of $M_{acc} = E_{cav}/(\varepsilon c^2)$ with a mean accretion rate of $\dot{M}_{acc} = M_{acc}/t_{sonic}$. Setting $\varepsilon = 0.1$, the mechanical outflow resulted from the accretion at least $2.86\,(\pm0.75)\times10^6$ M$_\odot$ of matter at a rate of 0.054 ± 0.004 M$_\odot$ yr^{-1}. For comparison, the mass accretion rate required to power the quasar is $\dot{M}_{acc}^{QSO} = L_{bol}^{QSO}/(\varepsilon c^2) \approx 14$ M$_\odot$ yr$^{-1} \approx 0.6\dot{M}_{Edd}$, dwarfing the mass accretion rate needed to power the jets. However, if M_{BH} grows as $(1-\varepsilon)\dot{M}_{acc}^{QSO}$, it will double in ≈ 80 Myr, and for I09 to adhere to the Magorrian relation, $> 10^{11}$ M$_\odot$ of stars would need to form, $> 10\%$ of the current bulge mass. This seems unlikely, so while the jets can subsist on a sub-Eddington accretion rate, the current period of quasar activity cannot, and thus is likely fleeting.

8.2 Hot and Cold Gas Accretion

The origin of the gas driving the nuclear activity cannot be precisely known, but how it is accreted can be constrained. If the accretion flow feeding the SMBH is composed of the hot ICM, it can be characterized in terms of the Bondi accretion rate, which represents idealized spherical accretion of gas onto a compact object at the ambient sound speed,

$$\dot{M}_{Bon} = 0.013\ K_{Bon}^{-3/2}\left(\frac{M_{BH}}{10^9\ M_\odot}\right)^2 \approx 3.2\times10^{-4}\ M_\odot\ yr^{-1} \tag{4}$$

where K_{Bon} [keV cm^2] is the mean entropy of gas within the Bondi radius and $K_{Bon} = K_0$ was assumed. Only considering the demands of the jets, the Bondi ratio of such an accretion flow is $\dot{M}_{acc}/\dot{M}_{Bon} \approx 300$, disturbingly large and implying highly efficient hot gas accretion. The Bondi radius for I09 is unresolved, and K_{Bon} is likely less than K_0. But, for a Bondi ratio of at least unity,

[1] http://leda.univ-lyon1.fr/
[2] http://www.sdss.org/
[3] http://www.ipac.caltech.edu/2mass/

even assuming gas close to R_{Bon} is no cooler than 0.65 keV and $M_{BH} = 4 \times 10^9$ M$_\odot$, K_{Bon} must be $\lesssim 2$ keV cm^2, 6 times lower than K_0, on the order of galactic coronae (Sun et al. 2007). In terms of entropy, $t_{cool} \propto K^{3/2} kT_X^{-1}$ (Donahue et al. 2006), which suggests the accreting material will have $t_{cool} \lesssim 100$ Myr, a factor of ≈ 3.5 below the shortest ICM cooling time and of order the core free-fall (ff) time. But this creates the problems that the gas should fragment and form stars (since $t_{cool} \sim t_{ff}$), and is disconnected from cooling at larger radii, breaking the feedback loop (Soker 2006).

If cold-mode accretion (Pizzolato & Soker 2005) dominates instead, then the gas which becomes fuel for the AGN is distributed in the BCG halo and migrates to the bottom of the galaxy potential in the form of cold blobs and filaments (Pizzolato & Soker 2010; Pizzolato et al. 2010). Indeed, radial filaments and gaseous substructure within 30 kpc of I09 are seen down to the resolution-limit of *HST* (Armus et al. 1999). This may indicate the presence of cooling, overdense regions similar to those expected in the cold-mode accretion model. Though Bondi accretion cannot be ruled out, it does not seem viable (which may be true in general, McNamara et al. 2010) and the process of cold-mode accretion appears to be more consistent with the nature of I09.

9   EVOLUTION OF THE FEEDBACK MODE?

AGN have three primary channels for interacting with their environment – jets, non-relativistic winds, and radiation pressure – and it is suspected these channels are active at different phases in a galaxy's evolution. The jets from I09 are clearly impacting the X-ray halo, and below we argue that winds and radiation may be affecting gas within the galaxy. It is plausible that all three AGN channels are simultaneously active in I09, further pointing to I09 as a rare transition object in the AGN feedback paradigm. In this section we also discuss the quasar misalignment, and suggest reasons it may be related to evolution of the feedback mode.

9.1   Non-Relativistic Winds

I09's status as a ULIRG, and its $> 10^{42}$ erg s^{-1} Hα luminosity (Crawford & Vanderriest 1996; Evans et al. 1998), would suggest that the galaxy hosts $> 10^{10}$ M$_\odot$ of cold gas (*e.g.* Sanders et al. 1988; Edge 2001). But, the cold H$_2$ mass of I09 is $< 10^{10}$ M$_\odot$ (Evans et al. 1998), there is $< 10^8$ M$_\odot$ of cold dust (Deane & Trentham 2001), the hot dust mass is $\sim 10^9$ M$_\odot$ (Taniguchi et al. 1997), and no polycyclic aromatic hydrocarbon (Taniguchi et al. 1997; Sargsyan et al. 2008) or silicate absorption features (Peeters et al. 2004) are detected in the galaxy's IR spectrum. Though the lack of PAHs may not be salient since the huge IR luminosity may dilute their signal. In spite of being a ULIRG BCG in a cool core cluster, I09 appears to be relatively gas-poor with a low gas-to-dust ratio.

One possible explanation for the apparent lack of cold gas in I09 is that non-relativistic winds are driving outflows which have broken apart the gas reservoirs (*e.g.* Hopkins & Elvis 2010). Rapid and extensive dust formation is expected in such winds (Elvis et al. 2002), and this could in part also explain the dust richness of I09. Outflows of varying speeds are found in many AGN host galaxies (see Crenshaw et al. 2003, for a review), and indeed, integral field spectroscopy indicates the presence of a > 1000 km s^{-1} emission line outflow coincident with the I09 nucleus (Crawford & Vanderriest 1996). Further, the CO upper limits found by Evans et al. (1998) do not exclude the existence of

a high-velocity (> 1500 km s^{-1}) component which could result from strong shocks driven by winds (*e.g.* Feruglio et al. 2010). The model of Lapi et al. (2005) predicts a quasar driven gas outflow will have a kinetic power of $L_{kin} \approx 0.05 L_{bol}^{QSO}$, with a total energy $E_{kin} \approx L_{kin} t_{QSO}$ where t_{QSO} is the quasar lifetime. For simplicity, assume t_{QSO} is less than the age of the AGN outburst (see Section 7), giving $L_{kin} \sim 10^{45}$ erg s^{-1} and $E_{kin} \sim 10^{60}$ erg. If this energy exceeds the thermal energy of the I09 intergalactic medium, then it is possible highly supersonic, small-scale shocks are being driven through the galaxy, thereby coupling ambient gas to the winds and amplifying their influence.

9.2   Radiation

Using a flux-limited sample of AGN selected from the *Swift*-BAT catalog, Fabian et al. (2009, hereafter F09) argue that radiation pressure has a significant influence on dusty gas clouds in a galaxy hosting an AGN. The F09 study compares the measured obscuring column density of each host galaxy with its effective Eddington ratio, $\lambda_{Edd} = L_{bol}^{QSO}(1.38 \times 10^{38} M_{BH})^{-1}$ erg^{-1} s M$_\odot$, which accounts for the effects of dust in decreasing the standard Eddington luminosity of a compact object (*e.g.* Laor & Draine 1993). F09 present a plot of $N_{H,obs}$-λ_{Edd} which is divided into regions where obscuring clouds are either long-lived, expelled, or appear as dust lanes.

In the formalism of F09, I09 has $\lambda_{Edd} \approx 0.55$, and in the $N_{H,obs}$-λ_{Edd} plane, resides toward the far-side of the long-lived region nearer the expulsion region than most other systems of similar $N_{H,obs}$. We find it reasonable to suspect that gas with a sight line to the quasar is being accelerated away from the quasar by radiation pressure, and is possibly being heated as well. These conclusions are, however, at the mercy of our choice for M_{BH} and assumed L_{bol}^{QSO}. For example, if $M_{BH} \geqslant 4 \times 10^9$ M$_\odot$ and $L_{bol}^{QSO} \sim 4 \times 10^{46}$ erg s^{-1}, then $\lambda_{Edd} < 0.08$, pushing I09 deeper into the long-lived region of the $N_{H,obs}$-λ_{Edd} plane, though still with a higher λ_{Edd} than AGN of similar $N_{H,obs}$.

9.3   Origin of Quasar Misalignment

H93 and H99 discuss in detail that the misalignment between the large-scale radio jets and beamed nuclear radiation may be correlated with evolution of the radio source from a FR-II to FR-I, and that the jet axis realignment must have transpired in less than a few Myrs. One simple explanation for the misalignment is that there are multiple SMBHs in the nucleus, each with its own accretion system and beaming axis. We could be seeing emission from two separate systems: one in quasar-mode, another in radio-mode. If multiple nuclei are a common feature of massive galaxies, which tend to experience a higher incidence of galaxy mergers and thus may be more likely to have more than one central SMBH, the implication is that a single AGN may not be wholly responsible for the evolution of the galaxy, and models should incorporate this property.

Alternatively, the misalignment may arise from a single SMBH having undergone a "spin-flip" (Merritt & Ekers 2002) which is hypothesized to occur when two black holes merge and the final black hole spin axis (believed to be synonymous with the radiation beaming axis) is drastically reoriented (*e.g.* Hodges-Kluck et al. 2010). However, black hole mergers may be lengthy (few Gyrs) and difficult processes which produce high-velocity kicks sufficient to eject the final black hole from even a massive galaxy (*e.g.* Campanelli et al. 2007). In addition, the spin

axes of merging black holes may naturally align when in a relatively gas-rich environment like I09's (Bogdanović et al. 2007). There are, however, 6 spheroids within a projected 80 kpc of I09 which may be companion galaxy remnants (Soifer et al. 1996; Armus et al. 1999), so there is the possibility that one or more mergers has taken place in the last few Myrs.

However, if there have been recent mergers, it is odd that the I09 radio source is very linear and highly-structured, and that the ICM appears to be so relaxed. Mergers have been implicated in producing long-lived X-ray substructures such as cold fronts and shocks (see Markevitch & Vikhlinin 2007, for a review) and inducing ICM bulk motions and turbulence that disrupt the flow of jet plasma, resulting in deformed radio sources (*e.g.* Simionescu et al. 2009, 2010). Yet I09 possesses none of these characteristics. It appears then, that if the misalignment arose via a merger, it either occurred prior to jet emergence or completely avoided the jets. The merger must also have been gentle so as not to stir the ICM.

The spin evolution framework of Garofalo et al. (2010, hereafter GES) provides another intriguing explanation which does not necessarily require mergers but instead relies on mass accretion. The GES model suggests that the evolution of a black hole's spin state is specifically correlated with a transition of the associated radio source from a powerful FR-II to lower-power FR-I. In the GES model, during the process of retrograde accretion induced spin-down, a black hole should pass through a state where the spin is ≈ 0. At this point, if there is an asymmetric accretion flow exceeding a M_{BH}-dependent critical M_{acc}, the spin axis can be dramatically reoriented on relatively short timescales (Cavagnolo et al. 2010, in preparation), possibly giving rise to the type of beamed jet-radiation misalignment observed in I09.

10 SUMMARY

In this paper we have shown that the QSO/AGN in IRAS 09104+4109 is interacting with its environment through both the mechanical and radiative feedback pathways. For the first time, we have a direct measurement of the radiative to mechanical feedback ratio in a single system, and may be peaking into the process of how massive galaxies at higher redshifts evolve from quasar-mode into radio-mode. It must be noted that, taken individually, I09 appears to be a normal BCG, a normal obscured quasar, a normal radio galaxy, residing in a normal cluster. It just so happens I09 is all these things at once. The individual results of this paper are as follows:

• Global and radial ICM analyses of the cluster hosting I09 do not reveal any X-ray properties or substructure to suggest RX J0913.7+4056 is anything but an unremarkable, massive, cool-core galaxy cluster.

• The nuclear X-ray source of I09 is well-described as reflected emission from cold matter illuminated by a $> 4 \times 10^{46}$ erg s^{-1} quasar obscured by moderately Compton-thick ($> 10^{24}$ cm^{-2}) matter.

• Detection and modeling of an X-ray excess NE of the nucleus indicates beamed quasar radiation is interacting with the ICM and a strongly photoionized nebulae in this same region.

• Cavities have been discovered in the X-ray halo of I09 which indicate the AGN outflow has a total mechanical power of $\approx 3 \times 10^{44}$ erg s^{-1}, which may be $\sim 10^{45}$ erg s^{-1} if significant gas shocking has occurred, and total energy output of $\approx 5 \times 10^{59}$ erg.

• The mass accretion rates required to power the QSO/AGN suggest that the fuel feeding the SMBH was likely not accreted directly from the hot ICM, *i.e.* via the Bondi mechanism, but rather

attained through the accretion of cold blobs of gas, *i.e.* via cold-mode accretion.

• Based on the presence of a quasar, interaction of the X-ray halo and jets, ostensible I09 gas-poorness, nuclear emission line outflow, high effective Eddington quasar luminosity, and misalignment of the large-scale radio jets and beamed radiation from the nucleus, we suggest that I09 is evolving from a radiation-dominated mode of feedback to a kinetic-dominated mode. Among other possible explanations, we speculate that the observed properties of I09 may be related to the process of SMBH spin evolution.

REFERENCES

Allen S. W., 2000, MNRAS, 315, 269 4

Anders E., Grevesse N., 1989, Geochim. Cosmochim. Acta, 53, 197 2

Armus L., Soifer B. T., Neugebauer G., 1999, Ap&SS, 266, 113 8, 9

Arnaud K. A., 1996, in Astronomical Society of the Pacific Conference Series, Vol. 101, Astronomical Data Analysis Software and Systems V, Jacoby G. H., Barnes J., eds., pp. 17–+ 2

Arnaud M., Aghanim N., Neumann D. M., 2002, A&A, 389, 1 3

Baldi A., Ettori S., Mazzotta P., Tozzi P., Borgani S., 2007, ApJ, 666, 835 6

Balestra I., Tozzi P., Ettori S., Rosati P., Borgani S., Mainieri V., Norman C., Viola M., 2007, A&A, 462, 429 6

Band D. L., Klein R. I., Castor J. I., Nash J. K., 1990, ApJ, 362, 90 5

Bassani L., Molina M., Malizia A., Stephen J. B., Bird A. J., Bazzano A., Bélanger G., Dean A. J., De Rosa A., Laurent P., Lebrun F., Ubertini P., Walter R., 2006, ApJ, 636, L65 2

Begelman M. C., Blandford R. D., Rees M. J., 1984, Reviews of Modern Physics, 56, 255 7

Binney J., Tabor G., 1995, MNRAS, 276, 663 1

Bîrzan L., McNamara B. R., Nulsen P. E. J., Carilli C. L., Wise M. W., 2008, ApJ, 686, 859 3, 7

Bîrzan L., Rafferty D. A., McNamara B. R., Wise M. W., Nulsen P. E. J., 2004, ApJ, 607, 800 2, 6, 7

Bogdanović T., Reynolds C. S., Miller M. C., 2007, ApJ, 661, L147 9

Bower R. G., Benson A. J., Malbon R., Helly J. C., Frenk C. S., Baugh C. M., Cole S., Lacey C. G., 2006, MNRAS, 370, 645 1

Campanelli M., Lousto C., Zlochower Y., Merritt D., 2007, ApJ, 659, L5 8

Cardelli J. A., Clayton G. C., Mathis J. S., 1989, ApJ, 345, 245 7

Carilli C. L., Perley R. A., Dreher J. W., Leahy J. P., 1991, ApJ, 383, 554 3

Cash W., 1979, ApJ, 228, 939 5

Cavagnolo K. W., Donahue M., Voit G. M., Sun M., 2008a, ApJ, 683, L107 4

—, 2008b, ApJ, 682, 821 4

—, 2009, ApJS, 182, 12 4

Cavagnolo K. W., McNamara B. R., Nulsen P. E. J., Carilli C. L., Jones C., Birzan L., 2010, arXiv e-prints: 1006.5699 7

Cavaliere A., Fusco-Femiano R., 1978, A&A, 70, 677 4

Churazov E., Brüggen M., Kaiser C. R., Böhringer H., Forman W., 2001, ApJ, 554, 261 1

Cohen A. S., Lane W. M., Cotton W. D., Kassim N. E., Lazio T. J. W., Perley R. A., Condon J. J., Erickson W. C., 2007, AJ, 134, 1245 3

Comastri A., Iwasawa K., Gilli R., Vignali C., Ranalli P., Matt G., Fiore F., 2010, arXiv e-prints: 1005.3253 5

Crawford C. S., Vanderriest C., 1996, MNRAS, 283, 1003 7, 8

Crenshaw D. M., Kraemer S. B., George I. M., 2003, ARA&A, 41, 117 8

Croton D. J., Springel V., White S. D. M., De Lucia G., Frenk C. S., Gao L., Jenkins A., Kauffmann G., Navarro J. F., Yoshida N., 2006, MNRAS, 365, 11 1

Dalla Bontà E., Ferrarese L., Corsini E. M., Miralda-Escudé J., Coccato L., Sarzi M., Pizzella A., Beifiori A., 2009, ApJ, 690, 537 7

De Young D. S., O'Neill S. M., Jones T. W., 2008, in Astronomical Society of the Pacific Conference Series, Vol. 386, Extragalactic Jets: Theory and Observation from Radio to Gamma Ray, T. A. Rector & D. S. De Young, ed., pp. 343–+ 2

Deane J. R., Trentham N., 2001, MNRAS, 326, 1467 8

Dekel A., Birnboim Y., 2006, MNRAS, 368, 2 1

Di Matteo T., Springel V., Hernquist L., 2005, Nature, 433, 604 1

Diehl S., Statler T. S., 2006, MNRAS, 368, 497 4

Donahue M., Horner D. J., Cavagnolo K. W., Voit G. M., 2006, ApJ, 643, 730 8

Donahue M., Voit G. M., 1993, ApJ, 414, L17 6

Dubinski J., 1998, ApJ, 502, 141 1

Dunn R. J. H., Fabian A. C., 2006, MNRAS, 373, 959 2

—, 2008, MNRAS, 385, 757 7

Edge A. C., 2001, MNRAS, 328, 762 8

Ehlert S., Ulmer M. P., 2009, A&A, 503, 35 6

Elvis M., Marengo M., Karovska M., 2002, ApJ, 567, L107 8

Evans A. S., Sanders D. B., Cutri R. M., Radford S. J. E., Surace J. A., Solomon P. M., Downes D., Kramer C., 1998, ApJ, 506, 205 2, 8

Faber S. M., Jackson R. E., 1976, ApJ, 204, 668 7

Fabian A. C., Crawford C. S., 1995, MNRAS, 274, L63 6

Fabian A. C., Iwasawa K., Reynolds C. S., Young A. J., 2000a, PASP, 112, 1145 5

Fabian A. C., Sanders J. S., Allen S. W., Crawford C. S., Iwasawa K., Johnstone R. M., Schmidt R. W., Taylor G. B., 2003, MNRAS, 344, L43 2

Fabian A. C., Sanders J. S., Ettori S., Taylor G. B., Allen S. W., Crawford C. S., Iwasawa K., Johnstone R. M., Ogle P. M., 2000b, MNRAS, 318, L65 2

Fabian A. C., Shioya Y., Iwasawa K., Nandra K., Crawford C., Johnstone R., Kunieda H., McMahon R., Makishima K., Murayama T., Ohashi T., Tanaka Y., Taniguchi Y., Terashima Y., 1994, ApJ, 436, L51 2

Fabian A. C., Vasudevan R. V., Mushotzky R. F., Winter L. M., Reynolds C. S., 2009, MNRAS, 394, L89 8

Ferland G. J., Korista K. T., Verner D. A., Ferguson J. W., Kingdon J. B., Verner E. M., 1998, PASP, 110, 761 6

Ferrarese L., Merritt D., 2000, ApJ, 539, L9 1

Feruglio C., Maiolino R., Piconcelli E., Menci N., Aussel H., Lamastra A., Fiore F., 2010, arXiv e-prints: 1006.1655 1, 8

Forman W., Jones C., Churazov E., Markevitch M., Nulsen P., Vikhlinin A., Begelman M., Böhringer H., Eilek J., Heinz S., Kraft R., Owen F., Pahre M., 2007, ApJ, 665, 1057 1

Franceschini A., Bassani L., Cappi M., Granato G. L., Malaguti G., Palazzi E., Persic M., 2000, A&A, 353, 910 2, 5

Garofalo D., Evans D. A., Sambruna R. M., 2010, MNRAS, 820 9

Gebhardt K., Bender R., Bower G., Dressler A., Faber S. M., Filippenko A. V., Green R., Grillmair C., Ho L. C., Kormendy J., Lauer T. R., Magorrian J., Pinkney J., Richstone D., Tremaine S., 2000, ApJ, 539, L13 1

George I. M., Fabian A. C., 1991, MNRAS, 249, 352 5

Graham A. W., 2007, MNRAS, 379, 711 7

Graham A. W., Erwin P., Caon N., Trujillo I., 2001, ApJ, 563, Ll1 1

Granato G. L., Silva L., Monaco P., Panuzzo P., Salucci P., De Zotti G., Danese L., 2001, MNRAS, 324, 757 1

Guainazzi M., Matt G., Perola G. C., 2005, A&A, 444, 119 5

Heavens A. F., Meisenheimer K., 1987, MNRAS, 225, 335 3

Hines D. C., Schmidt G. D., Wills B. J., Smith P. S., Sowinski L. G., 1999, ApJ, 512, 145 2

Hines D. C., Wills B. J., 1993, ApJ, 415, 82 2, 3

Hodges-Kluck E. J., Reynolds C. S., Miller M. C., Cheung C. C., 2010, ApJ, 717, L37 8

Hopkins P. F., Elvis M., 2010, MNRAS, 401, 7 8

Hopkins P. F., Hernquist L., 2009, ApJ, 698, 1550 2

Hopkins P. F., Hernquist L., Cox T. J., Di Matteo T., Martini P., Robertson B., Springel V., 2005, ApJ, 630, 705 1

Hopkins P. F., Hernquist L., Cox T. J., Di Matteo T., Robertson B., Springel V., 2006, ApJS, 163, 1 1

Iwasawa K., Fabian A. C., Ettori S., 2001, MNRAS, 321, L15 2, 5

Jaffe W. J., Perola G. C., 1973, A&A, 26, 423 3

Jones C., Forman W., 1984, ApJ, 276, 38 1

Kalberla P. M. W., Burton W. B., Hartmann D., Arnal E. M., Bajaja E., Morras R., Pöppel W. G. L., 2005, A&A, 440, 775 2

Kardashev N. S., 1962, Soviet Astronomy, 6, 317 3

Kauffmann G., Haehnelt M., 2000, MNRAS, 311, 576 1

Kereš D., Katz N., Weinberg D. H., Davé R., 2005, MNRAS, 363, 2 1

Kleinmann S. G., Hamilton D., Keel W. C., Wynn-Williams C. G., Eales S. A., Becklin E. E., Kuntz K. D., 1988, ApJ, 328, 161 2, 5

Kormendy J., Richstone D., 1995, ARA&A, 33, 581 1

Kriss G. A., Cioffi D. F., Canizares C. R., 1983, ApJ, 272, 439 4

Laor A., Draine B. T., 1993, ApJ, 402, 441 8

Lapi A., Cavaliere A., Menci N., 2005, ApJ, 619, 60 8

Lauer T. R., Faber S. M., Richstone D., Gebhardt K., Tremaine S., Postman M., Dressler A., Aller M. C., Filippenko A. V., Green R., Ho L. C., Kormendy J., Magorrian J., Pinkney J., 2007, ApJ, 662, 808 7

Leahy D. A., Creighton J., 1993, MNRAS, 263, 314 5

Magdziarz P., Zdziarski A. A., 1995, MNRAS, 273, 837 5

Magorrian J., Tremaine S., Richstone D., Bender R., Bower G., Dressler A., Faber S. M., Gebhardt K., Green R., Grillmair C., Kormendy J., Lauer T., 1998, AJ, 115, 2285 1

Markevitch M., Vikhlinin A., 2007, Phys. Rep., 443, 1 9

Mathur S., Stoll R., Krongold Y., Nicastro F., Brickhouse N., Elvis M., 2009, arXiv e-prints: 0910.3691 2

Matt G., Brandt W. N., Fabian A. C., 1996, MNRAS, 280, 823 5

Maughan B. J., 2007, ApJ, 668, 772 3

McNamara B. R., Nulsen P. E. J., 2007, ARA&A, 45, 117 1, 6

McNamara B. R., Rohanizadegan M., Nulsen P. E. J., 2010, arXiv e-prints: 1007.1227 8

McNamara B. R., Wise M., Nulsen P. E. J., David L. P., Sarazin C. L., Bautz M., Markevitch M., Vikhlinin A., Forman W. R., Jones C., Harris D. E., 2000, ApJ, 534, L135 2

Meier D. L., 2002, New Astronomy Review, 46, 247 7

Menci N., Fiore F., Puccetti S., Cavaliere A., 2008, ApJ, 686, 219 1

Merritt D., Ekers R. D., 2002, Science, 297, 1310 8

Mewe R., Gronenschild E. H. B. M., van den Oord G. H. J., 1985, A&AS, 62, 197 2

Miley G., 1980, ARA&A, 18, 165 3

Murphy K. D., Yaqoob T., 2009, MNRAS, 397, 1549 5

Nandra K., George I. M., Mushotzky R. F., Turner T. J., Yaqoob T., 1997, ApJ, 477, 602 5

Narayanan D., Cox T. J., Robertson B., Davé R., Di Matteo T., Hernquist L., Hopkins P., Kulesa C., Walker C. K., 2006, ApJ, 642, L107 1

Nousek J. A., Shue D. R., 1989, ApJ, 342, 1207 6

Pacholczyk A. G., 1970, Radio astrophysics. Nonthermal processes in galactic and extragalactic sources, Pacholczyk A. G., ed. 3

Peeters E., Spoon H. W. W., Tielens A. G. G. M., 2004, ApJ, 613, 986 8

Piconcelli E., Fiore F., Nicastro F., Mathur S., Brusa M., Comastri A., Puccetti S., 2007, A&A, 473, 85 5

Pizzolato F., Kelly T., Soker N., 2010, arXiv e-prints: 1007.3512 8

Pizzolato F., Soker N., 2005, ApJ, 632, 821 8

—, 2010, arXiv e-prints: 1003.4181 8

Poggianti B. M., 1997, A&AS, 122, 399 7

Polletta M., Omont A., Berta S., Bergeron J., Stalin C. S., Petitjean P., Giorgetti M., Trinchieri G., Srianand R., McCracken H. J., Pei Y., Dannerbauer H., 2008, A&A, 492, 81 1

Pratt G. W., Croston J. H., Arnaud M., Böhringer H., 2009, A&A, 498, 361 4

Rafferty D. A., McNamara B. R., Nulsen P. E. J., 2008, ApJ, 687, 899 4

Rafferty D. A., McNamara B. R., Nulsen P. E. J., Wise M. W., 2006, ApJ, 652, 216 2, 7

Reiprich T. H., Böhringer H., 2002, ApJ, 567, 716 4

Rengelink R. B., Tang Y., de Bruyn A. G., Miley G. K., Bremer M. N., Roettgering H. J. A., Bremer M. A. R., 1997, A&AS, 124, 259 3

Riley J. M. W., Waldram E. M., Riley J. M., 1999, MNRAS, 306, 31 3

Russell H. R., Fabian A. C., Sanders J. S., Johnstone R. M., Blundell K. M., Brandt W. N., Crawford C. S., 2010, MNRAS, 402, 1561 6

Sanders D. B., Soifer B. T., Elias J. H., Madore B. F., Matthews K., Neugebauer G., Scoville N. Z., 1988, ApJ, 325, 74 8

Sanders J. S., 2006, MNRAS, 371, 829 4

Sanderson A. J. R., O'Sullivan E., Ponman T. J., 2009, MNRAS, 395, 764 4

Sargsyan L., Mickaelian A., Weedman D., Houck J., 2008, ApJ, 683, 114 8

Schawinski K., Lintott C. J., Thomas D., Kaviraj S., Viti S., Silk J., Maraston C., Sarzi M., Yi S. K., Joo S., Daddi E., Bayet E., Bell T., Zuntz J., 2009, ApJ, 690, 1672 1

Scheuer P. A. G., Williams P. J. S., 1968, ARA&A, 6, 321 3

Sijacki D., Springel V., di Matteo T., Hernquist L., 2007, MNRAS, 380, 877 2

Silk J., Rees M. J., 1998, A&A, 331, L1 1

Simionescu A., Roediger E., Nulsen P. E. J., Brüggen M., Forman W. R., Böhringer H., Werner N., Finoguenov A., 2009, A&A, 495, 721 9

Simionescu A., Werner N., Forman W. R., Miller E. D., Takei Y., Böhringer H., Churazov E., Nulsen P. E. J., 2010, arXiv e-prints: 1002.0395 9

Slee O. B., Roy A. L., Murgia M., Andernach H., Ehle M., 2001, AJ, 122, 1172 3

Soifer B. T., Neugebauer G., Armus L., Shupe D. L., 1996, AJ, 111, 649 9

Soker N., 2006, New Astronomy, 12, 38 8

Springel V., White S. D. M., Jenkins A., Frenk C. S., Yoshida N., Gao L., Navarro J., Thacker R., Croton D., Helly J., Peacock J. A., Cole S., Thomas P., Couchman H., Evrard A., Colberg J., Pearce F., 2005, Nature, 435, 629 1

Sun M., Jones C., Forman W., Vikhlinin A., Donahue M., Voit M., 2007, ApJ, 657, 197 8

Taniguchi Y., Sato Y., Kawara K., Murayama T., Mouri H., 1997, A&A, 318, L1 5, 8

Tran H. D., Cohen M. H., Villar-Martin M., 2000, AJ, 120, 562 5, 6, 7

Tremaine S., Gebhardt K., Bender R., Bower G., Dressler A., Faber S. M., Filippenko A. V., Green R., Grillmair C., Ho L. C., Kormendy J., Lauer T. R., Magorrian J., Pinkney J., Richstone D., 2002, ApJ, 574, 740 7

Tueller J., Baumgartner W. H., Markwardt C. B., Skinner G. K., Mushotzky R. F., Ajello M., Barthelmy S., Beardmore A., Brandt W. N., Burrows D., Chincarini G., Campana S., Cummings J., Cusumano G., Evans P., Fenimore E., Gehrels N., Godet O., Grupe D., Holland S., Kennea J., Krimm H. A., Koss M., Moretti A., Mukai K., Osborne J. P., Okajima T., Pagani C., Page K., Palmer D., Parsons A., Schneider D. P., Sakamoto T., Sambruna R., Sato G., Stamatikos M., Stroh M., Ukwata T., Winter L., 2010, ApJS, 186, 378 2

Valtchanov I., Pierre M., Willis J., Dos Santos S., Jones L., Andreon S., Adami C., Altieri B., Bolzonella M., Bremer M., Duc P., Gosset E., Jean C., Surdej J., 2004, A&A, 423, 75 6

Veilleux S., Cecil G., Bland-Hawthorn J., 2005, ARA&A, 43, 769 1

Vikhlinin A., Kravtsov A., Forman W., Jones C., Markevitch M., Murray S. S., Van Speybroeck L., 2006, ApJ, 640, 691 4

Vikhlinin A., Markevitch M., Murray S. S., Jones C., Forman W., Van Speybroeck L., 2005, ApJ, 628, 655 4

Voit G. M., Cavagnolo K. W., Donahue M., Rafferty D. A., McNamara B. R., Nulsen P. E. J., 2008, ApJ, 681, L5 4

Waters C. Z., Zepf S. E., 2005, ApJ, 624, 656 3

Zdziarski A. A., Lubinski P., Smith D. A., 1999, MNRAS, 303, L11 5

Table 1. SUMMARY OF GLOBAL ICM SPECTRAL FITS.

Region	R_{in}	R_{out}	kT_X	L_{bol}	Z	$\chi^2_{red.}$	D.O.F.	% Source	η	Ct. Rate
-	kpc	kpc	keV	10^{44} erg s^{-1}	$Z_\odot$	-	-	-	10^{-4} cm^{-5}	ct s^{-1}
(1)	(2)	(3)	(4)	(5)	(6)	(7)	(8)	(9)	(10)	(11)
$R_{500-Core}$	174	1160	$7.54^{+1.76}_{-1.15}$	$6.90^{+0.61}_{-0.59}$	$0.38^{+0.31}_{-0.17}$	1.01	277	27	$8.24^{+6\%}_{-6\%}$	0.063
$R_{1000-Core}$	174	820	$6.80^{+1.14}_{-0.88}$	$6.17^{+0.41}_{-0.57}$	$0.38\dagger$	1.05	219	38	$7.90^{+3\%}_{-3\%}$	0.058
$R_{2500-Core}$	174	519	$7.18^{+1.25}_{-0.93}$	$5.18^{+0.41}_{-0.38}$	$0.38\dagger$	1.06	150	56	$6.48^{+3\%}_{-3\%}$	0.048
R_{500}	13	1160	$5.61^{+0.32}_{-0.30}$	$24.8^{+2.9}_{-2.5}$	$0.43^{+0.09}_{-0.08}$	0.78	357	54	$34.1^{+2\%}_{-2\%}$	0.237
R_{1000}	13	820	$5.49^{+0.28}_{-0.26}$	$24.2^{+2.6}_{-2.4}$	$0.40^{+0.08}_{-0.08}$	0.80	306	68	$33.8^{+2\%}_{-2\%}$	0.232
R_{2500}	13	519	$5.50^{+0.27}_{-0.25}$	$23.1^{+2.5}_{-2.0}$	$0.39^{+0.07}_{-0.07}$	0.82	265	83	$32.4^{+2\%}_{-2\%}$	0.222
R_{cool}	13	128	$4.94^{+0.24}_{-0.22}$	$16.1^{+2.5}_{-2.0}$	$0.42^{+0.08}_{-0.08}$	0.89	208	98	$22.9^{+3\%}_{-3\%}$	0.155

A dagger ($\dagger$) indicates core-excised regions fit with Z fixed at the iteratively determined value for $R_{500-Core}$. Bolometric luminosities were determined using a diagonalized response function over the energy range 0.01-100.0 keV with 5000 linearly spaced energy channels. Col. (1) Spectral extraction region; Col. (2) Inner radius; Col. (3) Outer radius; Col. (4) Gas temperature; Col. (5) Unabsorbed bolometric luminosity; Col. (6) Gas abundance; Col. (7) Reduced χ^2; Col. (8) Degrees of freedom; Col. (9) Percentage of emission attributable to source; Col. (10) Model normalization; Col (11) Background-subtracted count rate.

Table 2. SUMMARY OF NUCLEAR SOURCE SPECTRAL FITS.

Component	Parameter	SP09	SP99
(1)	(2)	(3)	(4)
PEXRAV	Γ	$1.71^{+0.23}_{-0.65}$	fixed to SP09
-	η_P	$8.07^{+0.64}_{-0.62} \times 10^{-4}$	$8.46^{+2.08}_{-2.12} \times 10^{-4}$
GAUSSIAN 1	E_G	$0.73^{+0.05}_{-0.24}$	$0.61^{+0.10}_{-0.05}$
-	σ_G	85^{+197}_{-53}	97^{+150}_{-97}
-	η_G	$8.14^{+3.74}_{-5.82} \times 10^{-6}$	$1.65^{+1.52}_{-1.00} \times 10^{-5}$
GAUSSIAN 2	E_G	$1.16^{+0.19}_{-0.33}$	$0.90^{+0.17}_{-0.90}$
-	σ_G	383^{+610}_{-166}	506^{+314}_{-262}
-	η_G	$1.03^{+3.22}_{-0.48} \times 10^{-5}$	$1.48^{+2.68}_{-1.16} \times 10^{-5}$
GAUSSIAN 3	E_G	$4.45^{+0.04}_{-0.04}$	$4.46^{+0.04}_{-0.07}$
-	σ_G	45^{+60}_{-45}	31^{+94}_{-31}
-	η_G	$2.67^{+0.91}_{-0.86} \times 10^{-6}$	$6.45^{+4.17}_{-3.69} \times 10^{-6}$
-	$EW^{corr}_{K\alpha}$	531^{+211}_{-218}	1210^{+720}_{-710}
Statistics	χ^2	79.0	7.9
-	DOF	74	15

Fe Kα equivalent widths have been corrected for redshift. Units for parameters: Γ is dimensionless, η_P is in photons keV^{-1} cm^{-2} s^{-1}, E_G are in keV, σ_G are in eV, η_G are in photons cm^{-2} s^{-1}, EW_{corr} are in eV. Col. (1) XSPEC model name; Col. (2) Model parameters; Col. (3) Values for 2009 *CXO* spectrum; Col. (4) Values for 1999 *CXO* spectrum.

Table 3. SUMMARY OF X-RAY EXCESSES SPECTRAL FITS.

Region	kT_X	η	E_G	σ_G	η_G	Cash	DOF
-	keV	10^{-5} cm^{-5}	keV	keV	10^{-6} cm^{-2} s^{-1}	-	-
(1)	(2)	(3)	(4)	(5)	(6)	(7)	(8)
EEx	$3.03^{+1.19}_{-0.74}$	$5.80^{+1.07}_{-0.97}$	-	-	-	524	430
EEx	$3.68^{+3.34}_{-1.58}$	$2.73^{+0.98}_{-0.94}$	[0.89, 1.42, 4.23]	[0.04, 0.16, 3.6E − 4]	[1.2, 2.0, 0.16]	384	430
EEx Bgd	$3.92^{+0.35}_{-0.31}$	$39.9^{+0.18}_{-0.17}$	-	-	-	471	430
WEx	$2.55^{+2.61}_{-0.98}$	$0.66^{+0.11}_{-0.07}$	-	-	-	387	430

Metal abundance was fixed at 0.5 $Z_\odot$ for all fits. Col. (1) Extraction region; Col. (2) Thermal gas temperature; Col. (3) Model normalization; Col. (4) Gaussian central energies; Col. (5) Gaussian dispersions; Col. (6) Gaussian normalizations; Col. (7) Modified Cash statistic; Col. (8) Degrees of freedom.

Table 4. SUMMARY OF CAVITY PROPERTIES.

Cavity	r	l	t_{sonic}	t_{buoy}	t_{refill}	pV	E_{cav}	P_{cav}
−	kpc	kpc	10^6 yr	10^6 yr	10^6 yr	10^{58} ergs	10^{59} ergs	10^{44} ergs s^{-1}
(1)	(2)	(3)	(4)	(5)	(6)	(7)	(8)	(9)
NW	6.40	58.3	50.5 ± 7.6	84.1 ± 10.3	158 ± 20	5.78 ± 1.07	2.31 ± 0.43	1.45 ± 0.35
SE	6.81	64.0	55.4 ± 8.4	92.2 ± 11.2	172 ± 21	6.99 ± 1.29	2.80 ± 0.52	1.60 ± 0.38

Col. (1) Cavity location; Col. (2) Radius of excavated cylinder; Col. (3) Length of excavated cylinder; Col. (4) Sound speed age; Col. (5) Buoyant rise time age; Col. (6) Volume refilling age; Col. (7) pV work; Col. (8) Cavity enthalpy; Col. (9) Cavity power using sonic age.
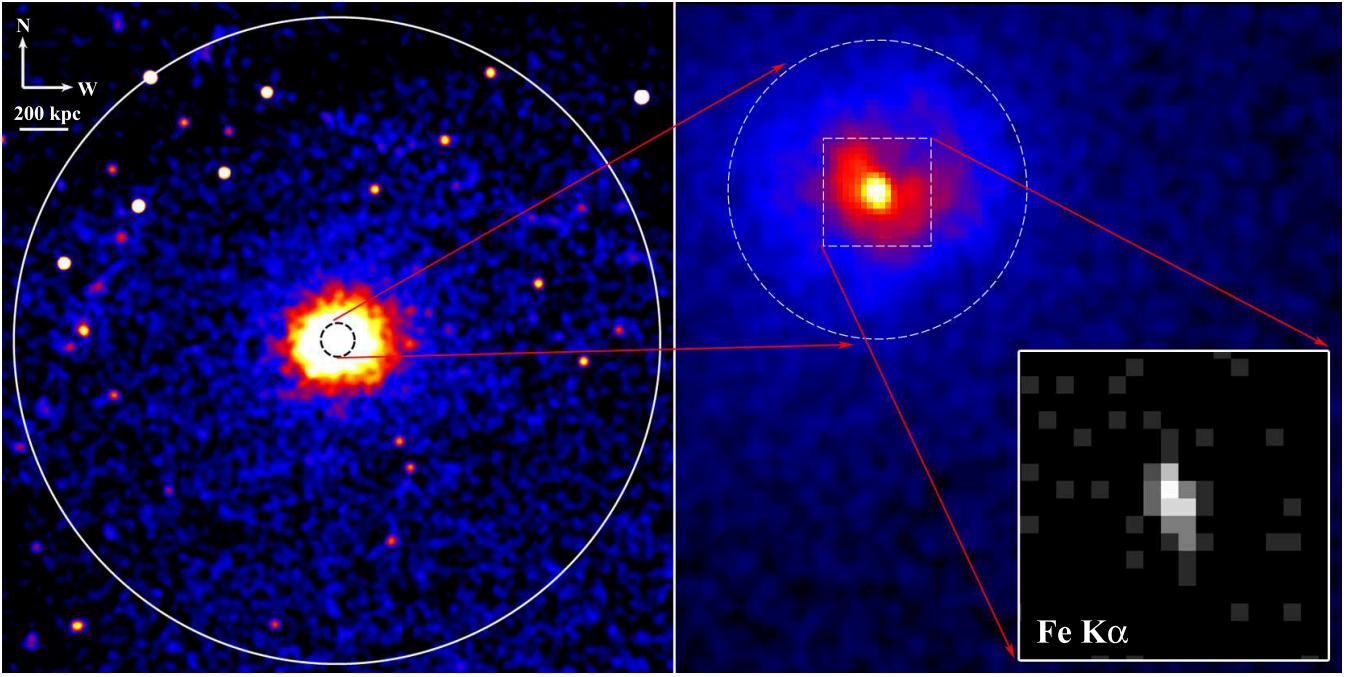
Figure 1. *Left*: *CXO* 0.5-10.0 keV exposure-corrected mosaic image of the RX J0913.7+4056 ICM. Image is smoothed with 5″ Gaussian. White circle marks R_{500} and dashed region has a diameter of 140 kpc. *Right*: Zoom-in of the core region smoothed with a 1″ Gaussian. Dashed box is 25 kpc on a side. The presence of cavity like structures to the NW and SE of the nucleus are evident. *Inset:* Events in the energy range 4.35-4.5 keV associated with the redshifted Fe Kα fluorescence line emission from the nucleus. Areas in black have 0 ct, and the darkest gray areas have 1 ct. The extent of the source is consistent with the *CXO* PSF, *i.e.* the source is not extended.
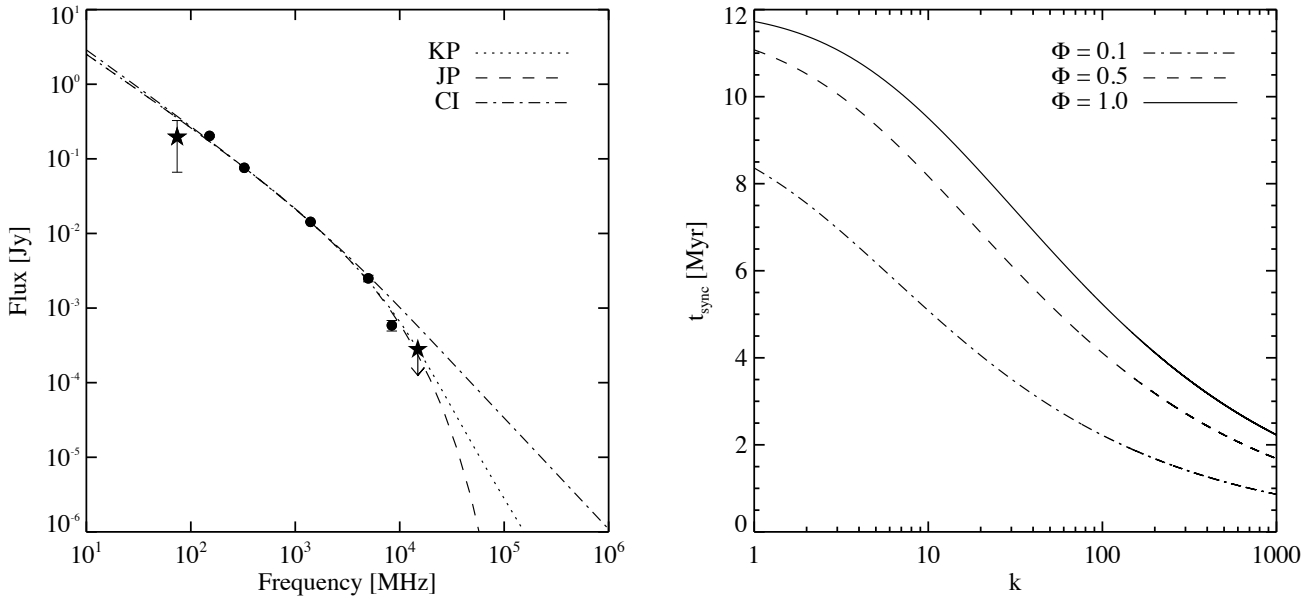
Figure 2. *Left*: Best-fit synchrotron models (see Section 2.2 for descriptions) for the radio spectrum of I09. Stars denote points excluded in fitting (see Section 2.2). Plotted fluxes are for the full radio source (nucleus, jets, and lobes), and the uncertainties are 1σ. The 1σ upper limit for the 14.9 GHz flux is shown. *Right*: Synchrotron age as a function of k, the ratio of lobe energy in non-radiating particles to that in relativistic electrons, for three values of Φ, the volume filling factor of the radiating particle population.
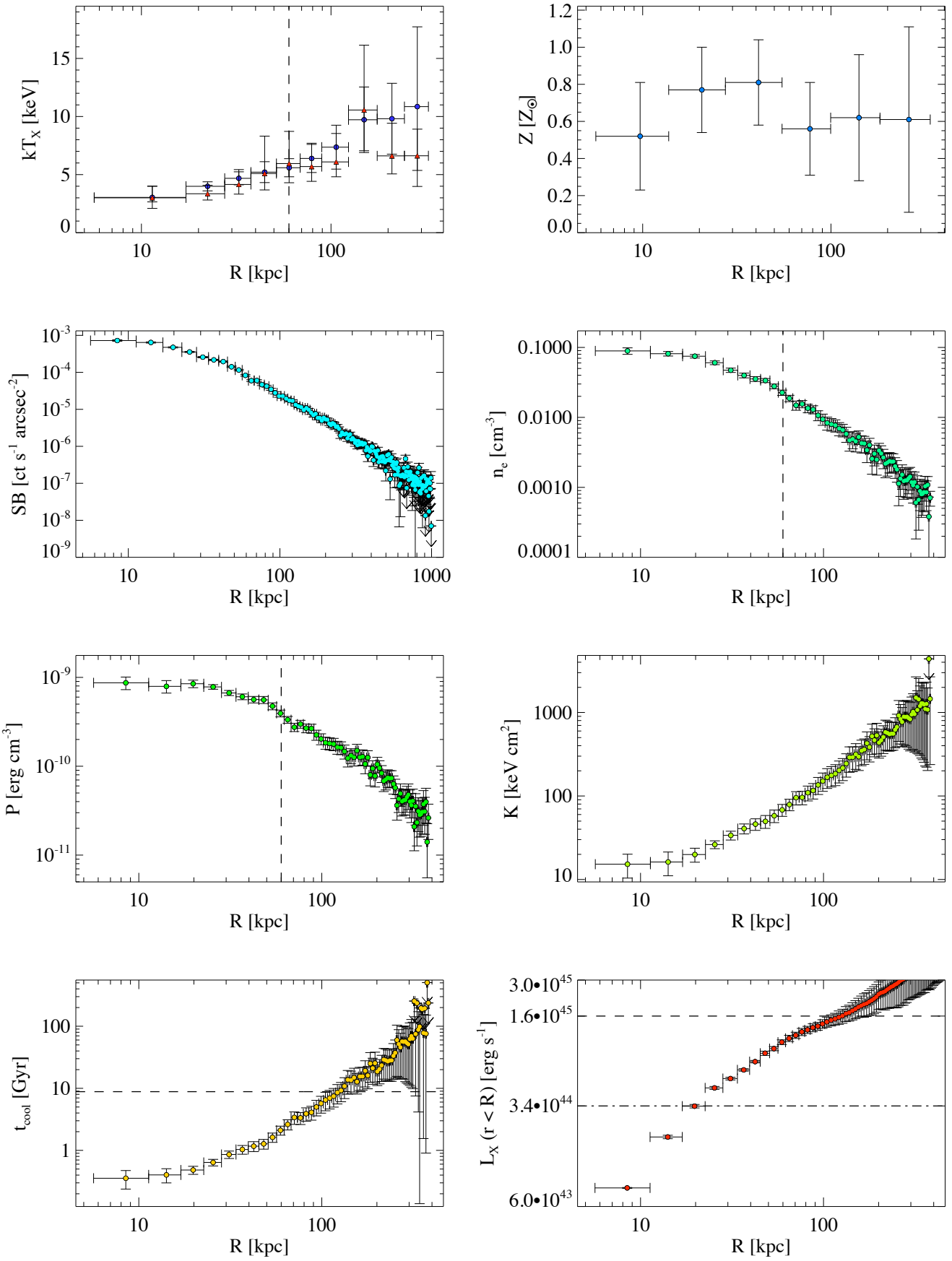
Figure 3. Gallery of radial ICM profiles. Vertical black dashed lines mark the approximate end-points of cavities. Horizontal dashed line in t_{cool} profile marks H_0^{-1} at $z = 0.4418$. For L_X profile, dashed line marks L_{cool}, and dashed-dotted line marks total P_{cav}.
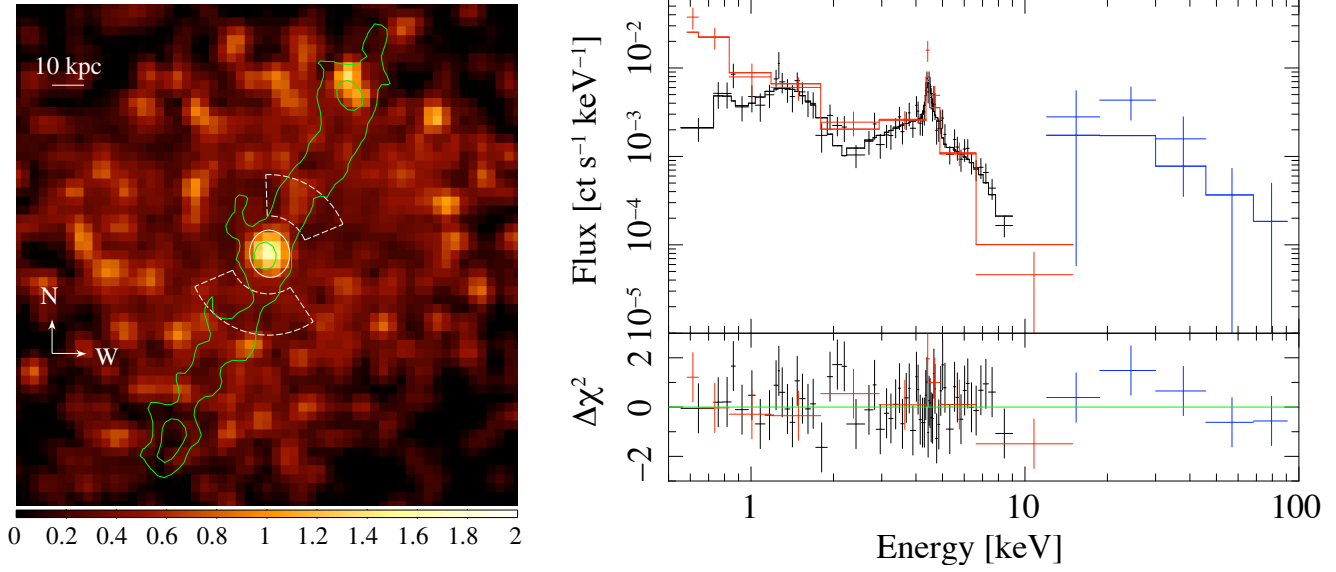
Figure 4. *Left:* X-ray *HR* map of the RX J0913.7+4056 core. Green contours trace the highest and lowest significance 1.4 GHz emission regions. White ellipse is the 90% EEF source region and dashed white wedges are background regions. The areas with the largest *HR* are coincident with the central source and the termination point of the northern radio jet. *Right:* Background-subtracted nuclear spectrum and best-fit model for the 1999 (red) & 2009 (black) *CXO* data and 1998 *BeppoSAX* PDS data (blue). Data has been binned to 3σ significance. The significant flux difference below 1.3 keV is a result of the greater effective area of the ACIS-S3 CCD in 1999 versus ACIS-I3 in 2009.
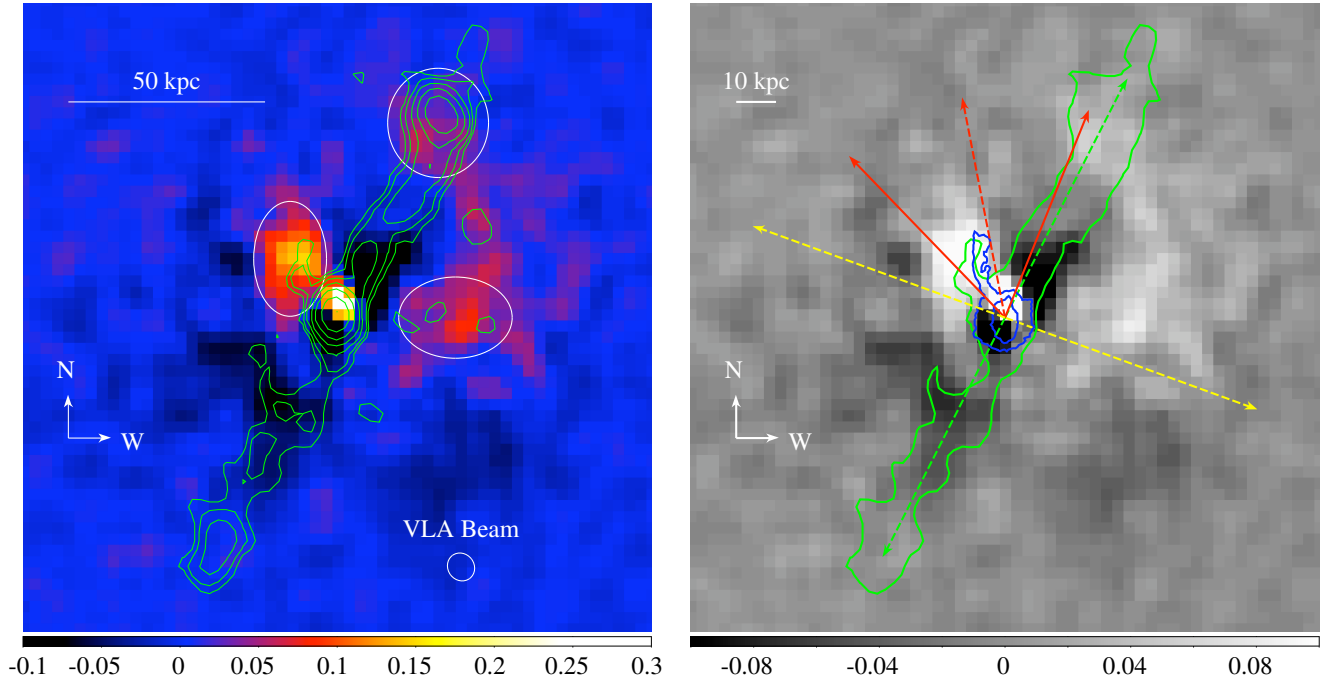

Figure 5. *Left*: Residual *CXO* X-ray image. Green contours trace 1.4 GHz radio emission in log-space steps beginning at $3\sigma_{RMS}$ and ending at 4.7 mJy beam^{-1}. The three white ellipses highlight regions of interest which are discussed in Section 6. The regions are illustrative and approximate the constant SB contours used to define the spectral extraction regions. *Right*: Same residual X-ray image as left panel, but in gray-scale. The green contour traces 1.4 GHz radio emission at $3\sigma_{RMS}$, and the dashed green line shows the jet axis. Blue contours trace $\lambda_{\mathrm{rest}} \approx 3900 - 6650$ Å emission as seen with *HST*. The red dashed line shows the mean direction of the UV scattering bicone (see H99 for discussion), while the solid red lines show the 1σ limits of the bicone opening angle.
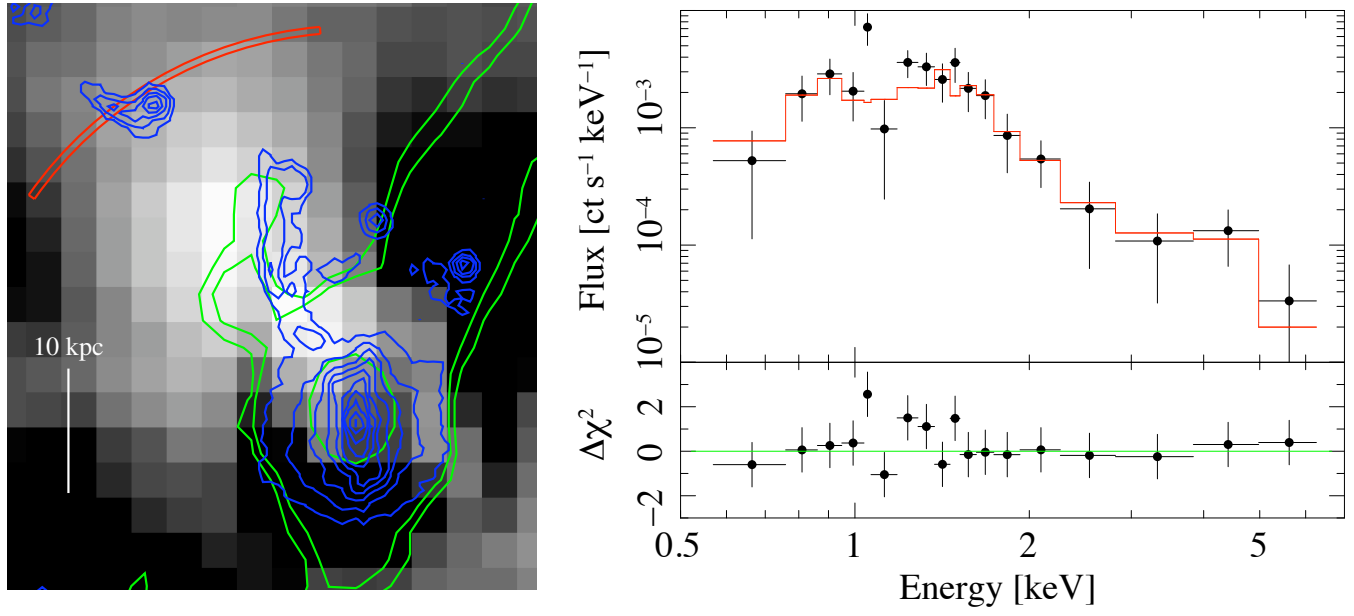
Figure 6. *Left:* Zoom-in of EEx overlaid with radio (green) and optical (blue) contours. Red wedge marks the extent of scattered UV emission. *Right:* Background-subtracted EEx spectrum binned to 3σ significance. The red line is the best-fit CLOUDY model for a QSO irradiated nebula and ICM.